

Combined Radar and Communications with Phase-Modulated Frequency Permutations

Tian Han, *Student Member, IEEE*, Rajitha Senanayake, *Member, IEEE*,

Peter Smith, *Fellow, IEEE*, Jamie Evans, *Senior Member, IEEE*,

William Moran, *Member, IEEE*, and Robin Evans, *Life Fellow, IEEE*

Abstract

This paper focuses on the combined radar and communications problem and conducts a thorough analytical investigation on the effect of phase and frequency change on the communication and sensing functionality. First, we consider the classical stepped frequency radar waveform and modulate data using M -ary phase shift keying (MPSK). Two important analytical tools in radar waveform design, namely the ambiguity function (AF) and the Fisher information matrix (FIM) are derived, based on which, we make the important conclusion that MPSK modulation has negligible effect on radar local accuracy. Next, we extend the analysis to incorporate frequency permutations and propose a new signalling scheme in which the mapping between incoming data and waveforms is performed based on an efficient combinatorial transform called the Lehmer code. We also provide an efficient communications receiver based on the Hungarian algorithm. From the communications perspective, we consider the optimal maximum likelihood (ML) detector and derive the union bound and nearest neighbour approximation on the block error probability. From the radar sensing perspective, we discuss the broader structure of the waveform based on the AF derivation and quantify the radar local accuracy based on the FIM.

Index Terms

Joint radar and communications, maximum likelihood, ambiguity function, Fisher information matrix.

I. INTRODUCTION

The integration of radar sensing and communication is a design paradigm in which sensing and communication functionalities share the same hardware and spectrum resources. Traditionally, communications and radar sensing were designed separately to focus on domain specific

challenges. However, as communication systems start to use the millimeter-wave (mmWave) frequency band, which is traditionally used in radar, there has been an increasing amount of research interest in the integration of the two functionalities [1]–[7]. Such joint systems can contribute to reducing the system cost and power consumption, as well as alleviating concerns for spectrum congestion [8]. It serves many new application scenarios such as connected and autonomous vehicles (CAVs) [9], [10], unmanned aerial vehicles (UAVs) [11], [12] and defence applications where both communications and radar sensing play important roles.

A. Related Works

A key aspect of the co-existence of the two functions in an integrated system is the design of a joint waveform that is capable of transmitting information and performing radar sensing simultaneously. The existing literature proposes several techniques to achieve the integration. Some research focuses on the realisation of the radar function based on the signal formats of the communication system [5]. In [13], the IEEE 802.11ad-based waveform which is traditionally used for wireless local area networks (WLANs) is proposed for long-range radar (LRR) applications at the 60 GHz unlicensed band. The preamble of this waveform, which consists of Golay complementary sequences with good correlation properties, is exploited to make it suitable for radar application. In [14], a virtual waveform design based on IEEE 802.11ad is proposed for an adaptive mmWave joint radar and communication system. The system transmits a few non-uniformly placed preambles to enhance the velocity estimation accuracy, at the cost of only a small reduction in the communication data rate. The use of orthogonal frequency division multiplexing (OFDM) waveforms for the joint system was considered in [15]–[17]. In [16], a wideband OFDM based waveform is presented and the high range resolution processing is derived. Furthermore, the impact of Doppler modulation on the processing is inspected to give recommendations of the OFDM parameters. In [17], the design of a power minimisation-based robust OFDM radar waveform is considered. However, due to the large number of subcarriers in an the OFDM waveform it introduces high peak-to-average power ratio (PAPR). This makes the approach challenging for typical radar operation since power amplifiers with a large linear range are required.

Research is also underway on the opposite design pattern, i.e., using traditional radar waveforms for data transmission. In [18], the famous linear frequency modulated (LFM) waveform is

considered for data transmission. However, the communication symbol rate corresponds to the chirp rate only, which is much lower than the symbol rate that can be achieved by a communication system in the same bandwidth. In [19], an M -ary frequency shift keying (MFSK) modulated chirp based radar and communication system is proposed, in which an FFT-based procedure is used to perform target detection. In [20], a phase-attached radar-communications (PARC) framework is extended to a frequency modulated continuous-wave (FMCW) implementation as a means to realise both functions. Stretch processing is employed such that large bandwidth radar operation and fine range resolution can be achieved. In [21], information sequences are implemented using continuous phase modulation (CPM) and phase-attached to a polyphase-coded frequency-modulated (PCFM) fixed radar waveform. The adjustable parameters provide control of the range side-lobe modulation (RSM) by trading off bit error rate (BER) and/or data throughput.

B. Motivations and Contributions

Despite the efforts made in these early designs for joint radar and communication systems, many fundamental research problems remain open. In this paper, we are motivated to conduct a rigorous theoretical analysis on the effect of phase and frequency modulation on the radar sensing functionality, which to the best of our knowledge is an important open problem.

One of the main challenges of embedding information into conventional radar waveforms is the limited rate of communication due to the lack of randomness. In addition, the radar estimation accuracy is sensitive to some parameters which might be varied during modulation and could cause degradation. Taking a different approach to the aforementioned papers, here, we focus on embedding data into the conventional stepped frequency radar waveform by randomising the parameters that have little effect on radar performance. We first consider the classical stepped frequency radar waveform and modulate data using PSK. Next, we extend the work in [22] by incorporating phase modulation into the random stepped frequency permutation waveform. This allows us to use both phase and frequency to modulate data and as a result transmit more data between nodes. We provide an analysis of both the communication and radar performances and make comparison with the waveform in [22].

Stepped frequency waveforms are commonly used in radar applications. A stepped frequency waveform has multiple subpulses, each with a constant frequency tone, but the frequencies

of different subpulses are equally separated by a constant step Δf Hz. Examples of stepped frequency radar waveforms include the linear stepped frequency waveform [23] and Costas coded waveform [24]. Phase coding is one of the early methods for pulse compression in radar applications [24]. Chirplike polyphase codes, such as Frank codes [25], have properties of low autocorrelation side-lobe levels and good Doppler tolerance. In [26], modified versions of Frank codes, namely P1 and P2 codes, are proposed. Compared to Frank codes, P1 and P2 codes are more tolerant of receiver bandlimiting prior to pulse compression. All of these waveforms, however, maintain a strict sequence of phase values carefully designed to achieve the best radar performance. As such, there is not enough randomness to modulate data, hence these waveforms are not suitable for the joint operation.

In this paper we focus on randomly changing the phase of each subpulse. Recently, in [27], an orthogonal frequency hopping multiple-input multiple-output (MIMO) radar waveform with PSK signalling is proposed, which shows that the highest side-lobe level of the AF is decreased due to phase modulation. However, the conclusion in this paper was drawn based on numerical simulations. In the current paper, we conduct a rigorous analytical investigation on the effect of phase and frequency change on the radar performance. The main contributions of this paper are as follows:

- First, we analyse the effect of phase modulation on the radar performance of the linear stepped frequency waveform. More specifically, we derive the AF, the Fisher information matrix (FIM) and approximations to the Cramer-Rao lower bounds (CRLBs) on delay and Doppler estimation error variances. Based on analytic tools, we discuss the impact of phase change on local accuracy and side-lobe levels of the AF.
- Next, we combine phase modulation and permutation of the frequency tones to propose a novel integrated radar and communication waveform. We present a new signalling scheme which allows more data to be transmitted and provide an efficient implementation for the mapping between the incoming data and the corresponding waveform based on a combinatorial transform called the Lehmer code. We derive the AF and discuss the broader structure of the waveform. We derive approximate expressions for the CRLBs on the delay and Doppler estimation errors based on the FIM, and provide a detailed evaluation of the local accuracy.
- From a communications perspective, we consider maximum likelihood (ML) detection and

analyse the error probability of the receiver in different wireless communication models. For additive white Gaussian noise (AWGN) channels and correlated Rician fading channels, we derive the union bound as well as the nearest neighbour approximation on the block error probability. In addition, we derive a new upper bound on the block error probability under the correlated Rayleigh fading model. To deal with the high complexity of an exhaustive search in ML detection, we provide an efficient ML receiver based on the Hungarian algorithm.

Extensive numerical examples are provided to illustrate the accuracy of our results.

II. PROBLEM FORMULATION

A. System Model

We consider a joint radar and communications system model where the transmitter sends a common waveform to both the radar target and the communications receiver. The signal reflected from the radar target is received and processed by the radar receiver, which is in the same location as the transmitter, to estimate the range and relative velocity of the target. The signal received at the communications receiver is processed to detect the transmitted information.

First, let us focus on the classical stepped frequency radar waveform with linearly increasing frequency tones. The complex envelope of such a stepped frequency radar waveform with L subpulses of length T can be given by

$$s(t) = \sqrt{\frac{E}{LT}} \sum_{l=0}^{L-1} s_p(t - lT) \exp(j2\pi f_l(t - lT)), \quad (1)$$

where the energy of the waveform $E = \int_0^{LT} |s(t)|^2 dt$ and $s_p(t)$ is a simple rectangular pulse

$$s_p(t) = \begin{cases} 1, & 0 \leq t \leq T \\ 0, & \text{otherwise.} \end{cases}$$

We also assume that the frequency tones are in ascending order and the difference between two successive frequency tones is $\Delta f = n/T$, where n is a positive integer. As such, the frequencies are orthogonal to each other and the frequency tone of the l -th subpulse can be expressed as

$$f_l = f_0 + n(l - 1)/T. \quad (2)$$

In (1), there are several parameters including the amplitude, phase and frequency of the waveform that can be changed in order to modulate data. In the current paper, we investigate novel methods of modulating the phase and frequency without causing significant changes to radar sensing

functionality. We keep the amplitude fixed because constant amplitude is extremely important for the efficient use of the power amplifiers in radar operation [23].

B. Radar Performance Measures

In this paper we focus on AF and FIM, the two key analytical tools used in radar waveform design. For convenience we have provided the definitions of these tools as follows.

The AF of a waveform describes the output of a matched filter when the signal input to the radar receiver is delayed and Doppler shifted by certain amounts. Based on [23, eq.(4.30)], the complex ambiguity function of the waveform $s(t)$ in (1) can be expressed as

$$\hat{A}(\tau, \omega) = \int_{-\infty}^{\infty} s(t)s^*(t - \tau)e^{j\omega t}dt, \quad (3)$$

where τ is the time delay to the expected matched filter peak output, and ω is the Doppler mismatch between the Doppler shift of the received signal and that for which the filter is designed. Then the AF is defined as the magnitude of the complex ambiguity function and is given by

$$A(\tau, \omega) = |\hat{A}(\tau, \omega)|. \quad (4)$$

The AF provides a measure of the degree of similarity between the transmitted waveform and its time and frequency shifted version [28]. The local accuracy can be analysed based on the shape of the AF around the origin, while the ambiguity can be studied by the AF side-lobe levels.

The FIM for delay and Doppler shift estimations provide a more detailed evaluation of the local accuracy of the waveform [28]. Consider the complex envelope of the radar received signal reflected by a single target, which can be written as

$$r_r(t) = \tilde{b}s(t - \tau)e^{j\omega t} + n(t), \quad (5)$$

where τ and ω are the target delay and Doppler shift to be estimated, \tilde{b} is a complex Gaussian random variable with zero mean and unit variance and $n(t)$ represents the baseband complex additive white Gaussian noise process with zero mean and power spectrum density N_0 [28, eq.(10.5)]. The Rayleigh fading variable, \tilde{b} , models the reflection from a target with multiple reflecting surfaces. The FIM for τ and ω is defined as

$$\mathbf{J} = \begin{bmatrix} J_{11} & J_{12} \\ J_{21} & J_{22} \end{bmatrix}, \quad (6)$$

where subscript 1 denotes τ and subscript 2 denotes ω . Using [28, eq.(10.63)-(10.65)], the elements of \mathbf{J} can be written as

$$J_{11} = C[\bar{\omega}^2 - \bar{\omega}^2], \quad (7)$$

$$J_{12} = J_{21} = C[\bar{\omega}\bar{\tau} - \bar{\omega}\bar{\tau}], \quad (8)$$

$$J_{22} = C[\bar{\tau}^2 - \bar{\tau}^2], \quad (9)$$

where $C = \frac{2}{N_0(1+N_0)}$, $\bar{\omega}^2$, $\bar{\omega}\bar{\tau}$ and $\bar{\tau}^2$ are given in [28, eq.(10.67)-(10.69)], respectively. Note that $\bar{\omega}$ and $\bar{\tau}$ can be calculated by replacing ω^2 with ω in [28, eq.(10.67)] and replacing u^2 by u in [28, eq.(10.69)], respectively. Based on the FIM elements we can derive the CRLBs on the delay and Doppler estimation errors.

III. PHASE MODULATED STEPPED FREQUENCY WAVEFORM

In this section, we introduce phase modulation to embed data into the waveform in (1). Suppose MPSK is used independently in each subpulse. Then, the waveform can be expressed as

$$s(t) = \sqrt{\frac{E}{LT}} \sum_{l=0}^{L-1} s_p(t - lT) \exp(j(2\pi f_l(t - lT) + \theta_l)), \quad (10)$$

where $\theta_l \in \{0, 2\pi/M, \dots, 2\pi(M-1)/M\}$ denotes the phase modulated into the l -th subpulse of the waveform. While adding MPSK allows us to send data, it impacts the radar sensing functionality. Thus, we proceed to analyse the AF and the FIM to discuss the effect of phase change on the radar performance.

A. Ambiguity Function

In order to derive the AF, we normalise the signal energy to one and re-express the waveform in (10) as

$$s(t) = \sqrt{\frac{1}{LT}} \sum_{l=0}^{M-1} s_p(t - lT) \exp(j(\omega_l(t - lT) + \theta_l)), \quad (11)$$

where $\omega_l = 2\pi f_l$ is the frequency in radians per second. Substituting (11) into (3) we can write the complex AF of $s(t)$ as

$$\hat{A}(\tau, \omega) = \frac{1}{LT} \sum_{l=0}^{L-1} \sum_{n=0}^{L-1} \int_{-\infty}^{\infty} s_p(s - lT) s_p^*(s - nT - \tau) e^{(j(\omega s + \omega_l(t - lT) - \omega_n(s - \tau - nT) + \theta_l - \theta_n))} ds. \quad (12)$$

Writing the complex AF of $s_p(t)$ as $\hat{A}_p(\tau, \omega)$ and rearranging (12) we obtain

$$\hat{A}(\tau, \omega) = \frac{1}{LT} \sum_{l=0}^{L-1} \sum_{n=0}^{L-1} \hat{A}_p(\tau + (n-l)T, \omega - (\omega_n - \omega_l)) e^{j(\omega_l T + \omega_n(\tau + (n-l)T) + (\theta_l - \theta_n))}, \quad (13)$$

where $\hat{A}_p(\tau, \omega)$ can be written as

$$\hat{A}_p(\tau, \omega) = \begin{cases} \frac{e^{j\omega(\tau+T)} - 1}{j\omega}, & -T < \tau < 0 \\ \frac{e^{j\omega T} - e^{j\omega\tau}}{j\omega}, & 0 \leq \tau < T \\ 0, & \text{otherwise.} \end{cases} \quad (14)$$

Next, by taking the magnitude of (13), we can write the AF of the waveform in (11) as

$$A(\tau, \omega) = \left| \frac{1}{LT} \sum_{l=0}^{L-1} \sum_{n=0}^{L-1} \hat{A}_p(\tau + (n-l)T, \omega - (\omega_n - \omega_l)) e^{j(\omega_l T + \omega_n(\tau + (n-l)T) + (\theta_l - \theta_n))} \right|. \quad (15)$$

The zero-Doppler cut of the AF describes the matched filter output when there is only time delay and no Doppler mismatch. By letting $\omega = 0$ in (15) we can obtain the zero-Doppler cut as

$$A(\tau, 0) = \left| \frac{1}{LT} \sum_{l=0}^{L-1} \sum_{n=0}^{L-1} \hat{A}_p(\tau + (n-l)T, \omega_l - \omega_n) e^{j(\omega_n(\tau - (n-l)T) + (\theta_l - \theta_n))} \right|. \quad (16)$$

Similarly, the zero-delay cut of the AF describes the matched filter output when there is no time delay, which can be found by letting $\tau = 0$ in (15) to derive

$$A(0, \omega) = \left| \frac{1}{LT} \sum_{l=0}^{L-1} \sum_{n=0}^{L-1} \hat{A}_p((n-l)T, \omega - (\omega_n - \omega_l)) e^{j(\omega_l T + \omega_n(n-l)T + (\theta_l - \theta_n))} \right|. \quad (17)$$

Due to the fact that $\hat{A}_p(\tau, \omega)$ in (14) is non-zero only when $-T < \tau < T$, it is obvious that $\hat{A}_p((n-l)T, \omega - (\omega_n - \omega_l))$ is non-zero only when $n = l$. Therefore, the zero-delay cut in (17) can be simplified as

$$A(0, \omega) = \left| \frac{1}{LT} \sum_{l=0}^{L-1} \hat{A}_p(0, \omega) e^{j\omega_l T} \right|, \quad (18)$$

which indicates that the zero-delay cut does not change with the phase modulation.

B. Fisher Information Matrix and Cramer-Rao Lower Bounds

Based on the definition of the FIM in (6) we proceed to derive the elements J_{11} , J_{12} , J_{21} and J_{22} as follows

$$J_{11} \approx \frac{2CB}{LT} \left(L - \sum_{l=0}^{L-2} \cos(\omega_l T + \theta_l - \theta_{l+1}) \right), \quad (19)$$

$$J_{12} = J_{21} \approx -\frac{CT^2}{2} \sum_{l=0}^{L-1} \omega_l (2l+1), \quad (20)$$

$$J_{22} = \frac{CL^2T^2}{12}, \quad (21)$$

where B is the finite bandwidth occupied by the rectangular pulse shaping function $s_p(t)$. The finite bandwidth B is introduced since $\overline{\omega^2}$ and $\bar{\omega}^2$ do not converge when $s_p(t)$ is a perfect rectangular pulse. The approximation in (19) is derived by neglecting small high order terms in the integrals which vanish when $BT \rightarrow \infty$ [22]. The detailed derivations of J_{11} , J_{22} and J_{12} are given in Appendices C, D and E, respectively.

The FIM is useful to bound the variance of the individual errors. More specifically, when unbiased estimators are used, the variances of delay and Doppler shift estimation errors are lower bounded by the diagonal elements in \mathbf{J}^{-1} [28]. Denoting the CRLBs of the delay estimation and Doppler shift estimation errors as CRLB_τ and CRLB_ω , respectively, their approximate expressions can be expressed as

$$\text{CRLB}_\tau \approx \frac{C^{-1}L^2T}{2LB \left(L - \sum_{l=0}^{L-2} \cos(\omega_l T + \theta_l - \theta_{l+1}) \right) - 3T^3 \left(\sum_{l=0}^{L-1} (2l+1)\omega_l \right)^2}, \quad (22)$$

$$\text{CRLB}_\omega \approx \frac{24C^{-1}B \left(L - \sum_{l=0}^{L-2} \cos(\omega_l T + \theta_l - \theta_{l+1}) \right)}{2L^2T^2B \left(L - \sum_{l=0}^{L-2} \cos(\omega_l T + \theta_l - \theta_{l+1}) \right) - 3LT^5 \left(\sum_{l=0}^{L-1} (2l+1)\omega_l \right)^2}. \quad (23)$$

Note that (22) and (23) can be further simplified based on [28, eq.(10.94), (10.95)] to produce

$$\text{CRLB}_\tau \approx \frac{C^{-1}LT}{2B \left(L - \sum_{l=0}^{L-2} \cos(\omega_l T + \theta_l - \theta_{l+1}) \right)}, \quad (24)$$

$$\text{CRLB}_\omega \approx \frac{12C^{-1}}{L^2T^2}. \quad (25)$$

While the simplified expressions in (24) and (25) provide a looser bound compared to (22) and (23), they clearly show the effect of parameters on the estimation errors. The delay estimation error lower bound in (24) is inversely proportional to the product of the finite bandwidth B and the effective bandwidth $1/T$ of a single subpulse. The Doppler shift estimation error lower bound in (25) is inversely proportional to the square of the time duration of the whole waveform LT . To observe the effect of embedding data on local accuracy, we first derive the CRLBs for

stepped frequency waveforms without phase modulation by setting $\theta_m = 0$ in (24) and (25), which results in

$$\text{CRLB}_\tau \approx \frac{C^{-1}LT}{2B \left(L - \sum_{l=0}^{L-2} \cos(\omega_l T) \right)}, \quad (26)$$

$$\text{CRLB}_\omega \approx \frac{12C^{-1}}{L^2 T^2}. \quad (27)$$

Comparing the CRLBs in (26) and (27) with those in (24) and (25), it can be found that the phase modulation has exactly no effect on the simplified CRLB_ω while it has some influence on CRLB_τ . Nevertheless, the maximum value (when all $\cos(\cdot)$ terms equal 1) and minimum value (when all $\cos(\cdot)$ terms equal -1) of the simplified CRLB_τ are kept unchanged when phase modulation is introduced. The discussions above are further analysed using numerical examples in Section III-C below.

C. Numerical Examples

In this section, we provide numerical examples to support the radar performance analyses in Section III-A and III-B. Fig. 1 to Fig. 3 illustrate the AF while Fig. 4 illustrates the CRLBs on delay and Doppler shift estimation errors.

Fig. 1 and Fig. 2 plot the AFs and the corresponding contour plots of the stepped frequency based waveforms without phase modulation and with phase modulation, respectively. The number of frequency tones $L = 8$. In Fig. 2, we consider quadrature phase shift keying (QPSK) modulation and set $M = 4$. We have given the plot for one random sequence of phases and this particular phase sequence will be used in all the plots for the phase modulated waveform in the remainder of this section. From Fig. 1 and Fig. 2 we observe that the broader structure of the AF is slightly changed due to the phase modulation. To be more specific, when there is no phase modulation, most of the volume under the AF is concentrated in a ridge located in the first and third quadrants. Although there still exists a ridge when phase modulation is introduced, the volume is slightly spread out. However, the AF around the origin is almost unaffected by the phase modulation.

To gain more insight into the AF and see the behaviour around the origin more clearly, Fig. 3 provides one dimensional cuts of the AFs in Fig. 1 and Fig. 2. From Fig. 3 (a) we observe that the zero-Doppler cut is changed due to the phase modulation but the change of the highest side-lobe

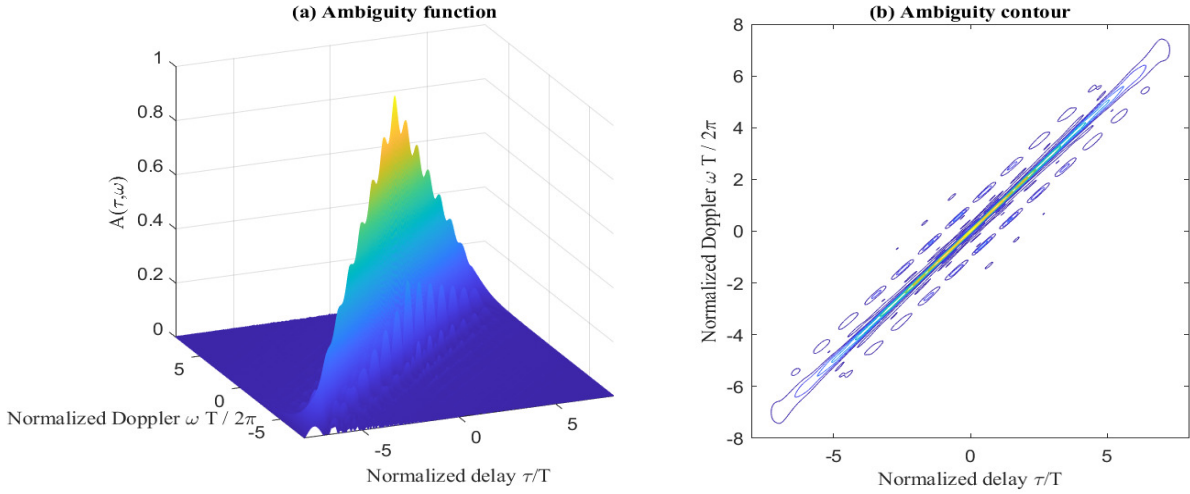


Fig. 1. The (a) three-dimensional surface plot and (b) contour plot of the AF of a linear stepped frequency waveform for $L = 8$. The first frequency $f_0 = 0$ Hz and the step $\Delta f = 1/\text{THz}$.

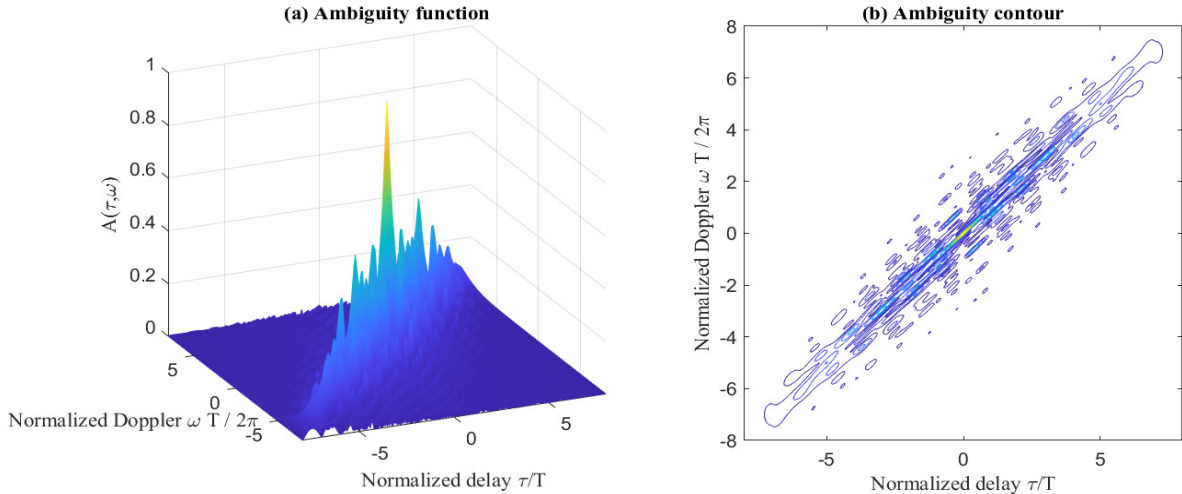


Fig. 2. The (a) three-dimensional surface plot and (b) contour plot of the AF of a linear stepped frequency and PSK based waveform for $L = 8$ and $M = 4$. The first frequency $f_0 = 0$ Hz and the step $\Delta f = 1/\text{THz}$. The phase sequence is $[3\pi/4, 3\pi/4, 3\pi/4, \pi/2, 3\pi/4, \pi/2, \pi/4, \pi/2]$.

level as well as the curvature at the origin is negligible, which indicates that phase modulation has little impact on the delay estimation accuracy. From Fig. 3 (b) we observe that the zero-delay cuts of the two AFs are exactly the same, which indicates that the phases of subpulses have no impact on the zero-delay cut. Hence, there is very little impact on the Doppler shift estimation accuracy. This also agrees with the theoretical results in (18) as well as the analysis in (25).

Next, we focus on quantitative performance measurements of the delay and Doppler shift

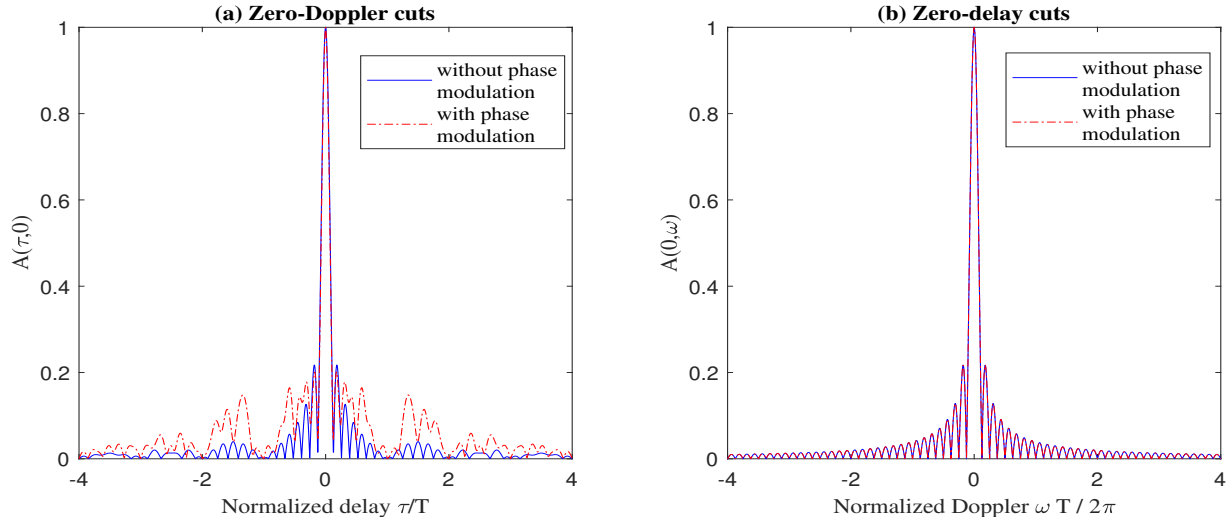


Fig. 3. The (a) zero-Doppler cuts and (b) zero-delay cuts of the AFs in Fig. 1 and Fig. 2.

estimation accuracies, which can be illustrated by the CRLBs. Fig. 4 (a) plots the the normalised CRLBs on delay estimation error in (24) and (26) versus the received signal-to-noise ratio (SNR). Fig. 4 (b) plots the normalised CRLBs on Doppler shift estimation error in (25) and (27) versus the received SNR. The waveforms we focus on are the same as those for Fig. 1 and Fig. 2. As is illustrated in Fig. 4 (a), the CRLB on delay estimation error decreases by changing the phases of subpulses. The approximated CRLB for the un-modulated stepped frequency waveform in (26) is maximised since $f_0 = 0$ Hz and $\Delta f = 1/T$ Hz, thus any phase change will result in a lower delay CRLB, as is shown by (24). Agreeing with (25), the CRLB on Doppler estimation error remains unchanged with phase modulation, as is illustrated in Fig. 4 (b).

IV. FREQUENCY PERMUTATIONS AND PHASE SHIFT KEYING BASED WAVEFORMS

In this section, we introduce a novel frequency modulation on top of the phase modulation introduced in Section III to embed more data into the waveform in (1). In the linear stepped frequency radar waveform considered in (10), the frequency was linearly changed according to (2). Motivated by [22], we proceed to change the order of frequency tones on top of the phase modulation, such that the randomisation in the frequency tones can be used to send more data. Interestingly, we observe that random permutation of the frequency tones results in a reasonably small AF side-lobe level in average and does not affect the AF around the origin.

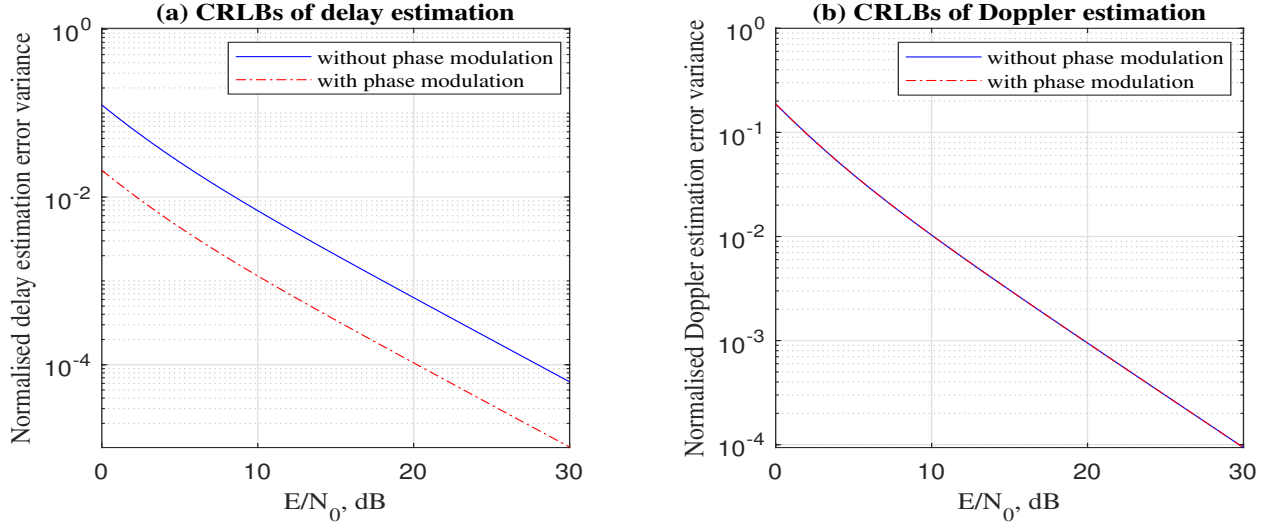


Fig. 4. The (a) approximated CRLBs in (24) and (26) on delay estimation errors and (b) approximated CRLBs in (25) and (27) on Doppler shift estimation errors for stepped frequency based waveforms with and without phase modulation..

A. Incorporating Frequency Permutations

Consider the sequence of L frequency tones f_0, f_1, \dots, f_{L-1} illustrated by (2). If a single frequency tone is used only once in a particular waveform having L subpulses, we can formulate $L!$ of these waveforms. The frequencies of the i -th waveform, $\{f_0^i, \dots, f_{L-1}^i\}$, follow the i -th permutation from a total of $L!$ permutation sequences where f_l^i denotes the frequency in the l -th slot of the i -th waveform. The i -th waveform can be expressed as

$$s_i(t) = \sqrt{\frac{E}{LT}} \sum_{l=0}^{L-1} s_p(t - lT) \exp(j(2\pi f_l^i(t - lT))). \quad (28)$$

To increase the achievable data rate, we introduce phase modulation which is performed independently of the frequency modulation. Suppose M -ary phase shift keying is used, we can formulate $L! \times M^L$ possible waveforms in total. The i -th waveform can now be expressed as:

$$s_i(t) = \sqrt{\frac{E}{LT}} \sum_{l=0}^{L-1} s_p(t - lT) \exp(j(2\pi f_l^i(t - lT) + \theta_l^i)), \quad (29)$$

where $\theta_l^i \in \{0, 2\pi/M, \dots, 2\pi(M-1)/M\}$ denotes the phase of the l -th subpulse of the i -th waveform and the frequencies of the i -th waveform follow one of the $L!$ permutations given by

$$\begin{aligned} \Psi_1 &= \dots = \Psi_{M^L} = \{f_0, \dots, f_{L-2}, f_{L-1}\} \\ \Psi_{M^L+1} &= \dots = \Psi_{2M^L} = \{f_0, \dots, f_{L-1}, f_{L-2}\} \\ &\vdots \\ \Psi_{(L!-1) \times M^L+1} &= \dots = \Psi_{L! \times M^L} = \{f_{L-1}, \dots, f_1, f_0\}. \end{aligned} \tag{30}$$

For simplicity we define $M_T = L! \times M^L$ to be the total number of possible waveforms.

B. Generation of the Waveforms

As has been discussed, we can formulate M_T possible waveforms under the novel modulation scheme in Section IV-A. When L and M are large, a huge look-up table is required to map the data to the waveform. However, we can avoid the use of the look-up table by implementing the mapping using the *Lehmer code* [29]. To be more specific, if the incoming data symbol is represented as an index i where $i \in \{1, \dots, M_T\}$, the integer $(\lfloor \frac{i-1}{M^L} \rfloor + 1)$ is mapped to a particular permutation of L frequency tones using a factorial number system as detailed in [22, Section II-C], where $\lfloor \cdot \rfloor$ denotes the operation of rounding the argument down. Then, the integer $(i - 1 - \lfloor \frac{i-1}{M^L} \rfloor M^L)$ is converted to a sequence of L digits with base number M and sent into a standard MPSK modulator to generate a particular sequence of L phases.

C. Ambiguity Function

In order to derive the AF, we normalise the signal energy to one and re-express the i -th waveform in (29) as

$$s_i(t) = \sqrt{\frac{1}{LT}} \sum_{l=0}^{L-1} s_p(t - lT) \exp(j(\omega_l^i(t - lT) + \theta_l^i)), \tag{31}$$

where $\omega_l^i = 2\pi f_l^i$ is the frequency in radians per second. Following similar steps as in Section III-A, we can write the AF of the waveform in (31) as

$$A(\tau, \omega) = \left| \frac{1}{LT} \sum_{l=0}^{L-1} \sum_{n=0}^{L-1} \hat{A}_p(\tau + (n-l)T, \omega - (\omega_n^i - \omega_l^i)) e^{j(\omega_l^i T + \omega_n^i (\tau + (n-l)T) + (\theta_l^i - \theta_n^i))} \right|, \tag{32}$$

The zero-Doppler cut and the zero-delay cut can be expressed as

$$A(\tau, 0) = \left| \frac{1}{LT} \sum_{l=0}^{L-1} \sum_{n=0}^{L-1} \hat{A}_p(\tau + (n-l)T, \omega_l^i - \omega_n^i) e^{j(\omega_n^i (\tau - (n-l)T) + (\theta_l^i - \theta_n^i))} \right|, \tag{33}$$

$$A(0, \omega) = \left| \frac{1}{LT} \sum_{l=0}^{L-1} \sum_{n=0}^{L-1} \hat{A}_p((n-l)T, \omega - (\omega_n^i - \omega_l^i)) e^{j(\omega_l T + \omega_n^i(n-l)T + (\theta_l^i - \theta_n^i))} \right|. \quad (34)$$

Similarly, the zero-delay cut in (34) can be simplified as

$$A(0, \omega) = \left| \frac{1}{LT} \sum_{l=0}^{L-1} \hat{A}_p(0, \omega) e^{j\omega l T} \right|, \quad (35)$$

which implies that the zero-delay cut is not affected by frequency permutation and phase change.

As is analysed in [22], the overall structure of the AF resulting from the random stepped frequency permutation based waveform has a narrow main-lobe and small side-lobes. When phase modulation is introduced, these good radar properties will not be affected much. Such an AF can achieve good radar performance specially with clutter. Since transmitter tends to send a waveform with a randomly selected frequency permutation due to the randomness of incoming information, we can consider that the clutter enters via the average AF side-lobe level which is reasonably small for our waveform. The performance of the AFs with different parameters will be further discussed using numerical examples in Section IV-E.

D. Fisher Information Matrix and Cramer-Rao Lower Bounds

In this section we follow similar steps as is used in Section III-B. Replacing ω_m and θ_m with ω_m^i and θ_m^i , respectively, the FIM elements can be approximated or expressed as

$$J_{11} \approx \frac{2CB}{LT} \left(L - \sum_{l=0}^{L-2} \cos(\omega_l^i T + \theta_l^i - \theta_{l+1}^i) \right), \quad (36)$$

$$J_{12} = J_{21} \approx -\frac{CT^2}{2} \sum_{l=0}^{L-1} \omega_l^i (2l+1), \quad (37)$$

$$J_{22} = \frac{CL^2 T^2}{12}. \quad (38)$$

Based on (36)-(38), the CRLBs of the delay estimation and Doppler shift estimation errors can be approximated by

$$\text{CRLB}_\tau \approx \frac{C^{-1} L^2 T}{2LB \left(L - \sum_{l=0}^{L-2} \cos(\omega_l^i T + \theta_l^i - \theta_{l+1}^i) \right) - 3T^3 \left(\sum_{l=0}^{L-1} (2l+1)\omega_l^i \right)^2}, \quad (39)$$

$$\text{CRLB}_\omega \approx \frac{24C^{-1} B \left(L - \sum_{l=0}^{L-2} \cos(\omega_l^i T + \theta_l^i - \theta_{l+1}^i) \right)}{2L^2 T^2 B \left(L - \sum_{l=0}^{L-2} \cos(\omega_l^i T + \theta_l^i - \theta_{l+1}^i) \right) - 3LT^5 \left(\sum_{l=0}^{L-1} (2l+1)\omega_l^i \right)^2}. \quad (40)$$

By ignoring J_{12} and J_{21} [28, eq.(10.94), (10.95)], (39) and (40) can be simplified to looser bounds, which can be expressed as

$$\text{CRLB}_\tau \approx \frac{C^{-1} LT}{2B \left(L - \sum_{l=0}^{L-2} \cos(\omega_l^i T + \theta_l^i - \theta_{l+1}^i) \right)}, \quad (41)$$

$$\text{CRLB}_\omega \approx \frac{12C^{-1}}{L^2 T^2}. \quad (42)$$

Again, the simplified expressions in (41) and (42) clearly show the effect of parameters on the estimation errors. The delay estimation error lower bound in (41) is inversely proportional to B and to the effective bandwidth, $1/T$, of a single subpulse. The Doppler shift estimation error lower bound in (42) is inversely proportional to the square of time duration of the whole waveform LT . In addition, compared to [22, eq.(48), (49)], it can be found that the phase modulation has exactly no effect on the simplified CRLB_ω while it does affect CRLB_τ . Similar to Section III-B, the maximum value and minimum value of CRLB_τ in (42) are kept unchanged when phase modulation is introduced. The analysis is supported by the numerical examples in Section IV-E.

E. Numerical Examples

In this section, we provide numerical examples to verify the theoretical analyses in Section IV-C and Section IV-D. Fig. 5 and Fig. 6 illustrate the AFs and the corresponding contour plots for the random frequency permutation based waveforms for $L = 8$ without phase modulation and with phase modulation, respectively. Both the frequency permutation and the phase sequence are randomly generated and will be fixed for the remainder of this section. We observe that the main-lobes of the AFs in Fig. 5 and Fig. 6 are very similar, which again implies that the phase modulation has negligible impact on the AF around the origin. In addition, by comparing Fig. 5 and Fig. 6 with Fig. 1 and Fig. 2, it can be observed that the frequency permutation has a larger impact on the broader structure of the AF than the phase modulation. By randomly choosing a frequency permutation, the volume under the AF is more likely to be evenly spread over the delay-Doppler plane as is evident by the side-lobe structure of Fig. 5 and Fig. 6 compared to that of a waveform with an ascending frequency sequence given in Fig. 1 and Fig. 2. This result shows the averaging effect on the AF side-lobe level discussed in Section IV-C, which supports the statement that the performance of this waveform with clutter is good on average.

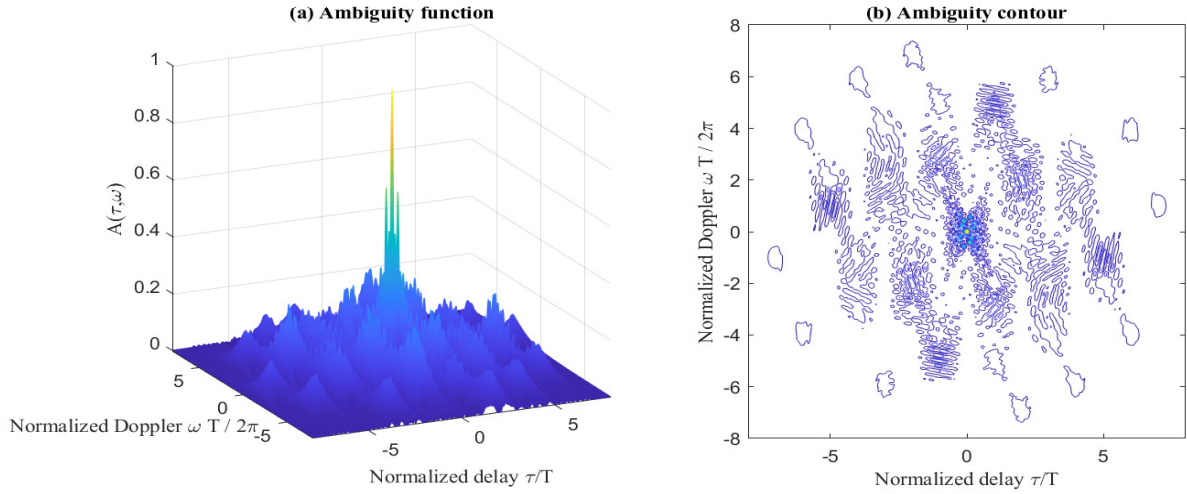


Fig. 5. AF of a frequency permutation based waveform for $L = 8$. The frequency sequence is $[f_2, f_7, f_5, f_0, f_4, f_1, f_6, f_3]$.

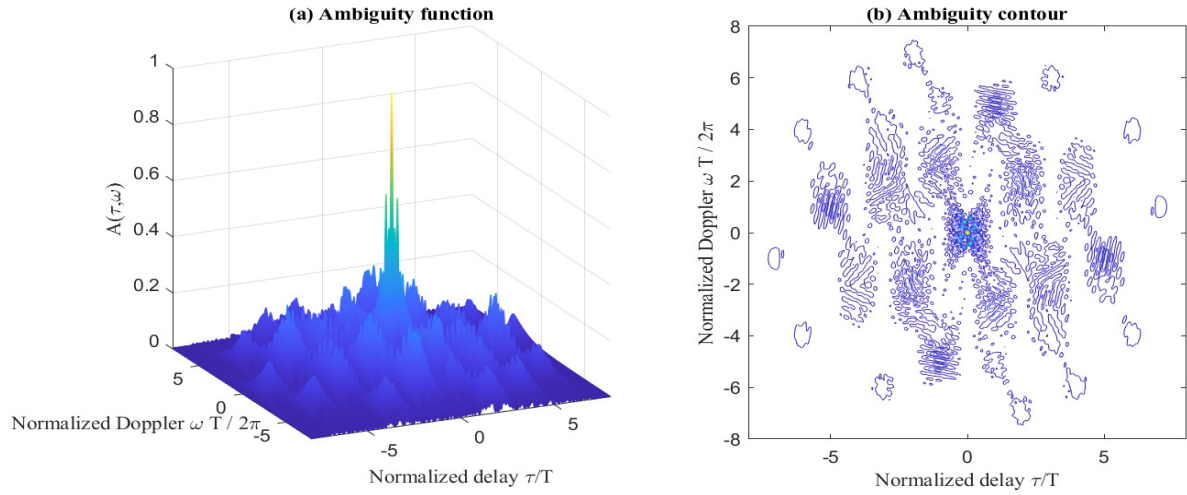


Fig. 6. AF of a frequency permutation and PSK based waveform for $L = 8$ and $M = 4$. The frequency sequence is $[f_2, f_7, f_5, f_0, f_4, f_1, f_6, f_3]$. The phase sequence is $[3\pi/4, 3\pi/4, 3\pi/4, \pi/2, 3\pi/4, \pi/2, \pi/4, \pi/2]$.

Fig. 7 plots the one dimensional cuts of the AFs in Fig. 5 and Fig. 6. The zero-Doppler cuts in Fig. 7 (a) indicate that the change due to the phase modulation in both the highest side-lobe level and the curvature at the origin is negligible. As is discussed in Section III-C, the zero-delay cut is not affected by the phase modulation, which can also be observed in Fig. 7 (b). Compared to Fig. 3, we notice that the frequency permutation does not affect the zero-delay cuts as well. This agrees with the expression in (35) as well as the analysis in (42).

Fig. 8 plots the the normalised CRLBs on delay estimation error in [22, eq.(48)] and (41), as

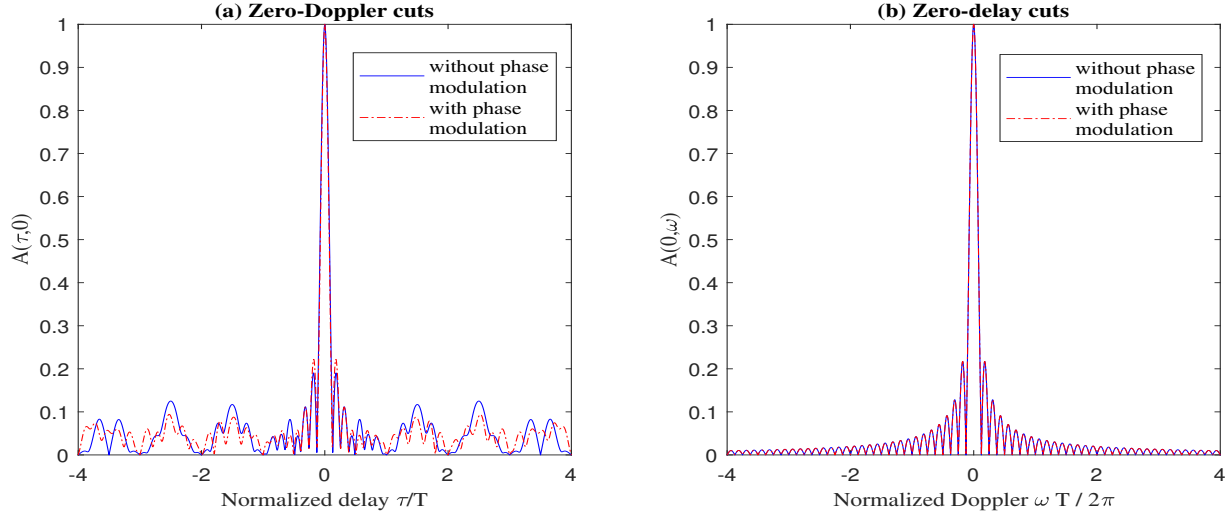


Fig. 7. The (a) zero-Doppler cuts and (b) zero-delay cuts of the AFs in Fig. 5 and Fig. 6.

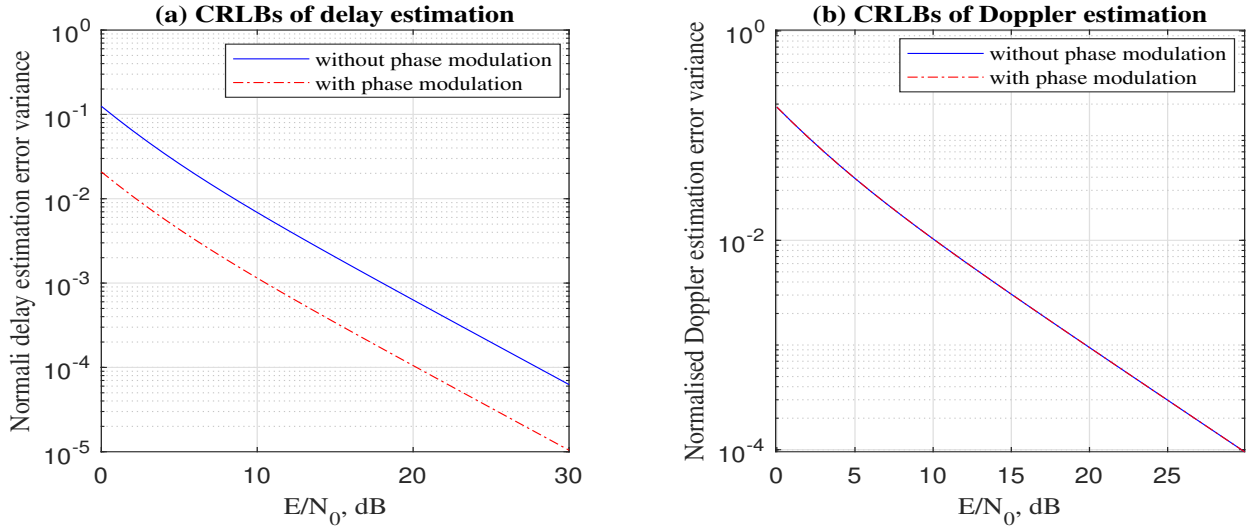


Fig. 8. The (a) approximated CRLBs in (41) on delay estimation errors and (b) approximated CRLBs in (42) on Doppler shift estimation errors for stepped frequency based waveforms with and without phase modulation..

well as the normalised CRLBs on Doppler shift estimation error in [22, eq.(49)] and (42) versus the received SNR, respectively. The waveforms we focus on are the same as those for Fig. 5 and Fig. 6. Since $f_0 = 0$ Hz and $\Delta f = 1/T$ Hz, the simplified CRLB_τ in (41) is maximised without phase modulation and is decreased due to the change of phases, which is shown in Fig. 8 (a). The simplified CRLB_ω in (42) remains unchanged with phase change, as is shown in Fig. 8 (b).

V. COMMUNICATIONS PERFORMANCE ANALYSIS

In this section, we focus on the communication performance of the joint radar and communication waveform. In Section III, we consider the traditional MPSK modulation for which the communication performance is quite well known and therefore is not discussed in this paper. In Section IV we consider combining MPSK modulation with frequency permutation, which results in a new signalling scheme. In this section we focus on this interesting new communication system and analyse its performance in terms of the block error probability. More specifically, we perform the optimal ML detection at the communication receiver and derive analytical expressions for the union bound, nearest neighbour approximation and a new upper bound on the block error probability. In addition, we propose the implementation of an efficient communication receiver based on the Hungarian algorithm.

A. Maximum Likelihood Detection

Assume there are N antennas at the communications receiver. The baseband received signal at time t can be represented by an $N \times 1$ vector

$$\mathbf{r}_c(t) = \mathbf{h}s_i(t) + \mathbf{n}(t), \quad (43)$$

where \mathbf{h} is the fading channel vector, $s_i(t)$ is the transmitted signal and $\mathbf{n}(t)$ is an AWGN vector in which the power spectral density (PSD) of each element is N_0 . The transmission of $s_i(t)$ is assumed to be equally likely among all M_T possible waveforms. Suppose the channel vector is known at the receiver, then ML detection of the received signal is given by

$$\begin{aligned} \hat{s}_i(t) &= \underset{s_k(t) \in \{s_1(t), \dots, s_{M_T}(t)\}}{\operatorname{argmin}} \int_0^{LT} |\mathbf{h}^H \mathbf{r}_c(t) - \mathbf{h}^H \mathbf{h} s_k(t)|^2 dt \\ &= \underset{s_k(t) \in \{s_1(t), \dots, s_{M_T}(t)\}}{\operatorname{argmax}} \Re \left\{ \int_0^{LT} s_k^*(t) \mathbf{h}^H \mathbf{r}_c(t) dt \right\}, \end{aligned} \quad (44)$$

where $\Re\{\cdot\}$ denotes the operation of taking the real part of the argument.

B. Error Probability Analysis

1) *AWGN channel*: The AWGN channel is one of the fundamental channel models. By assuming a unit channel gain, the fading vector satisfies $\mathbf{h}^H \mathbf{h} = N$. Suppose the i -th waveform, $s_i(t)$, is transmitted. Then the probability of the correct detection of $s_i(t)$ is given by

$$P_c(i) = \Pr \left[\xi_{ii} = \max_{k \in \{1, \dots, M_T\}} \xi_{ik} \right], \quad (45)$$

where ξ_{ik} is the k -th decision variable when $s_i(t)$ is transmitted, and is given by

$$\xi_{ik} = \Re \left\{ \int_0^{LT} s_k^*(t) \mathbf{h}^H \mathbf{r}_c(t) dt \right\}. \quad (46)$$

Since the transmission of each waveform is assumed to be equally likely, the average probability of making a wrong detection is

$$P_e = \frac{1}{M_T} \sum_{i=1}^{M_T} (1 - P_c(i)). \quad (47)$$

We note that it is difficult to calculate the exact expression of P_e since it requires multi-dimensional integrals. Therefore, we consider the union bound on P_e , which is given by

$$P_e \leq P_e^{UB} = \frac{1}{M_T} \sum_{i=1}^{M_T} \sum_{\substack{k=1, \\ k \neq i}}^{M_T} P_{ik}, \quad (48)$$

where P_{ik} denotes the pairwise error probability (PEP) that the k -th signal is preferred over the i -th signal when the i -th signal is transmitted and is given by

$$P_{ik} = \Pr [\xi_{ik} - \xi_{ii} \geq 0]. \quad (49)$$

Due to the symmetry of PEPs, we can further simplify the union bound as

$$P_e^{UB} = \sum_{k=2}^{M_T} P_{1k}. \quad (50)$$

Next we proceed to analyse P_{ik} . Similar to the derivations in [22, eq.(10)-(11)], by substituting (46) into (49) and rearranging the expressions, we obtain

$$P_{ik} = \Pr \left[\frac{E \left(L - \sum_{q=1}^{L-d} \cos(\theta_{l(q)}^k - \theta_{l(q)}^i) \right)}{L} \mathbf{h}^H \mathbf{h} < Z_1 \right], \quad (51)$$

where d is the number of frequency tones $s_i(t)$ and $s_k(t)$ differ by, $l(q)$ is the index of the q -th subpulse where $s_i(t)$ and $s_k(t)$ have the same frequency and $Z_1 = \Re \left\{ \mathbf{h}^H \int_0^{LT} (s_k^*(t) - s_i^*(t)) \mathbf{n}(t) dt \right\}$.

When conditioned on the channel fading, Z_1 is a Gaussian random variable with zero mean and variance $E \left(L - \sum_{q=1}^{L-d} \cos(\theta_{l(q)}^k - \theta_{l(q)}^i) \right) N_0 \mathbf{h}^H \mathbf{h} / L$. Thus we can express the PEP in (49) as

$$P_{ik} = \Pr \left[\sqrt{\mathbf{h}^H \mathbf{h}} \leq \alpha_{ik} Z \right], \quad (52)$$

where

$$\alpha_{ik} = \sqrt{\frac{LN_0}{E \left(L - \sum_{q=1}^{L-d} \cos(\theta_{l(q)}^k - \theta_{l(q)}^i) \right)}},$$

and $Z \sim \mathcal{N}(0, 1)$ is a standard Gaussian random variable. By setting $\mathbf{h}^H \mathbf{h} = N$, the pairwise error probability P_{ik} over the AWGN channel can be represented as

$$P_{ik} = Q\left(\frac{\sqrt{N}}{\alpha_{ik}}\right), \quad (53)$$

where $Q(\cdot)$ is the Gaussian Q-function. Substituting (53) to (50) we find the resulting union bound over the AWGN channel as

$$P_e^{UB} = \sum_{k=2}^{M_T} Q\left(\frac{\sqrt{N}}{\alpha_{1k}}\right). \quad (54)$$

We note that, if L and M are large, there are $M_T - 1$ pairwise error probabilities to be added up, which will make the union bound far above the exact error probability, especially in the low SNR region. To provide a better approximation, we derive the nearest neighbour approximation of the error probability, in which we only consider the pairwise error probabilities corresponding to the nearest neighbours [30]. When $M > 2$, the nearest neighbours of a particular waveform $s_i(t)$ are the waveforms with the same frequency permutation as $s_i(t)$, while the phase is only different in a single subpulse by the amount of $2\pi/M$. The number of nearest neighbours for a particular waveform is $2L$. Thus the nearest neighbour approximation can be expressed as

$$P_e^{NN} = 2LP_{1k}^{NN}, \quad (55)$$

where P_{1k}^{NN} is the PEP that the nearest neighbour $s_k(t)$ is preferred over $s_1(t)$ when $s_1(t)$ is transmitted, which can be expressed as

$$P_{1k}^{NN} = Q\left(\frac{\sqrt{N}}{\alpha_{ik}^{NN}}\right), \quad (56)$$

where

$$\alpha_{ik}^{NN} = \sqrt{\frac{LN_0}{E\left(1 - \cos\left(\frac{2\pi}{M}\right)\right)}}. \quad (57)$$

When $M = 2$, however, the set of nearest neighbours of a particular waveform $s_i(t)$ is the union of two subsets. The first subset has a size of L , which contains the waveforms with the same frequency permutation as $s_i(t)$, while the phase is only different in a single subpulse by the amount of π . In the second subset, the waveforms have $L - 2$ subpulses in the same positions as $s_i(t)$. For the other two subpulses, the order of the frequency tones are different compared to $s_i(t)$ while phases do not matter. The size of the second subset is $2L(L - 1)$. Therefore, when $M = 2$, the nearest neighbour approximation can be expressed as

$$P_e^{NN} = (2L^2 - L)P_{1k}^{NN}, \quad (58)$$

where P_{1k}^{NN} in (58) can be expressed by (56) with $a_{ik}^{NN} = \sqrt{\frac{LN_0}{2E}}$. Thus, the nearest neighbour approximation over the AWGN channel can be written as

$$P_e^{NN} = \begin{cases} 2LQ\left(\sqrt{\frac{NE(1 - \cos(2\pi/M))}{LN_0}}\right), & M > 2 \\ (2L^2 - L)Q\left(\sqrt{\frac{2NE}{LN_0}}\right), & M = 2. \end{cases} \quad (59)$$

2) *Correlated fading channels*: Under fading channels, we first focus on the correlated Rician fading channel with a line-of-sight (LOS) path and a scattered path. For such a system, the channel fading vector can be expressed as

$$\mathbf{h} = \sqrt{\frac{K}{K+1}}\Delta + \sqrt{\frac{1}{K+1}}\mathbf{R}_u^{1/2}\mathbf{u}, \quad (60)$$

where Δ denotes the $N \times 1$ complex LOS phase vector with the i -th element having the property $|\Delta_i|^2 = 1$, $\mathbf{u} \sim \mathcal{CN}(0, \mathbf{I}_N)$, K is the Rician factor which denotes the relative strength of the LOS path to the scattered path and \mathbf{R}_u denotes the $N \times N$ correlation matrix of the scattered component. As \mathbf{R}_u is a symmetric matrix it can be expressed as

$$\mathbf{R}_u = \mathbf{V}\boldsymbol{\Omega}\mathbf{V}^H, \quad (61)$$

where \mathbf{V} is unitary and $\boldsymbol{\Omega} = \text{diag}(\lambda_1, \dots, \lambda_N)$ is a diagonal matrix containing the eigenvalues $\lambda_1, \dots, \lambda_N$ of \mathbf{R}_u . We denote the j -th element of the vector $(\mathbf{V}^H\Delta)$ as $(\mathbf{V}^H\Delta)_j$. Whilst not given here due to page limitations, after lengthy mathematical manipulations, P_{1k} for correlated Rician channels can be derived as

$$P_{1k} = \frac{1}{\pi} \int_0^{\pi/2} \prod_{j=1}^N \left(\frac{2(K+1)\alpha_{1k}^2 \sin^2 \theta}{\lambda_j + 2(K+1)\alpha_{1k}^2 \sin^2 \theta} \right) \exp\left(-K \sum_{j=1}^N \frac{|(\mathbf{V}^H\Delta)_j|^2}{\lambda_j + 2(K+1)\alpha_{1k}^2 \sin^2 \theta}\right) d\theta. \quad (62)$$

and the full proof of the above derivation is included in Appendix A. Substituting (62) into (50), (55) and (58), we obtain the union bound as well as the nearest neighbour approximation of the error probability over a correlated Rician fading channel.

Next, we focus on the Rayleigh fading channel, which is a special case of the Rician fading channel. The fading vector \mathbf{h} for the Rayleigh channel does not have the LOS component, and is given by (60) with $K = 0$. Therefore, by setting $K = 0$ in (62), the pairwise error probability can be expressed as

$$P_{1k} = \frac{1}{\pi} \int_0^{\pi/2} \prod_{j=1}^N \left(\frac{2\alpha_{1k}^2 \sin^2 \theta}{\lambda_j + 2\alpha_{1k}^2 \sin^2 \theta} \right) d\theta. \quad (63)$$

As has been stated in Section V-B1, when L and M are large, the union bound can be very loose, especially in the low SNR regime. This problem becomes more severe in fading channels, since the channels are random vectors. Therefore, in the following we propose a tighter upper bound on the error probability for fading channels as

$$P_e \leq P_e^{NB} = \min_{\gamma \geq 0} \left\{ \Pr [\mathbf{h}^H \mathbf{h} < \gamma] + \Pr [\mathbf{h}^H \mathbf{h} \geq \gamma] \sum_{k=2}^{M_T} \tilde{P}_{1k} \right\}, \quad (64)$$

where γ is a threshold defined for the total channel gain and

$$\tilde{P}_{1k} = \Pr [\xi_{11} < \xi_{1k} \mid \mathbf{h}^H \mathbf{h} \geq \gamma]. \quad (65)$$

In (64), the bound is created by assuming that a detection error always occurs when the channel gain is lower than a defined threshold γ . The minimisation with respect to γ in (64) is taken to make the upper bound as tight as possible. Using the result in (52) and following the steps in Appendix B, (65) can be expressed as

$$\tilde{P}_{1k} = \frac{1}{\Pr [\mathbf{h}^H \mathbf{h} \geq \gamma]} \int_{\gamma}^{\infty} \frac{1}{\pi} \int_0^{\pi/2} e^{-\frac{x}{2\alpha_{1k}^2 \sin^2 \theta}} d\theta f_{\mathbf{h}^H \mathbf{h}}(x) dx, \quad (66)$$

where $f_{\mathbf{h}^H \mathbf{h}}(x)$ is the probability density function of $\mathbf{h}^H \mathbf{h}$.

For the correlated Rayleigh fading channel, we can rewrite $\mathbf{h}^H \mathbf{h}$ as

$$\mathbf{h}^H \mathbf{h} = \mathbf{u}^H \mathbf{R}_u \mathbf{u} \equiv \sum_{j=1}^N \lambda_j |\mathbf{u}_j|^2, \quad (67)$$

where \mathbf{u}_j is the j -th element of the vector \mathbf{u} and \equiv indicates statistical equivalence. Thus, the probability density function of the random variable in (67) can be expressed as [31]

$$f_{\mathbf{h}^H \mathbf{h}}^{\text{Ray}}(x) = \begin{cases} \sum_{j=1}^N \frac{b_j}{\lambda_j} e^{-x/\lambda_j}, & x \geq 0 \\ 0, & x < 0, \end{cases} \quad (68)$$

where $b_j = \lambda_j^{N-1} \prod_{\substack{n=1 \\ n \neq j}}^N 1/(\lambda_j - \lambda_n)$. Hence the cumulative distribution function of $\mathbf{h}^H \mathbf{h}$ is given by

$$F_{\mathbf{h}^H \mathbf{h}}^{\text{Ray}}(x) = \begin{cases} \sum_{j=1}^N b_j (1 - e^{-x/\lambda_j}), & x \geq 0 \\ 0, & x < 0. \end{cases} \quad (69)$$

Substituting (68) and (69) into (66) and (64), we can express the new upper bound over the correlated Rayleigh fading channel as

$$P_e^{NB} = \min_{\gamma \geq 0} \left\{ \sum_{j=1}^N b_j (1 - e^{-x/\lambda_j}) + \frac{1}{\pi} \sum_{k=2}^{M_T} \sum_{j=1}^N \frac{2b_j \alpha_{1k} \sin^2 \theta}{\lambda_j + 2\alpha_{1k} \sin^2 \theta} \int_0^{\pi/2} e^{-\gamma \left(\frac{1}{2\alpha_{1k} \sin^2 \theta} + \frac{1}{\lambda_j} \right)} d\theta \right\}. \quad (70)$$

C. Communications Receiver Implementation

In this section we propose the implementation of an efficient communications receiver for the novel signalling scheme presented in Section IV. The optimal receiver based on the ML detection rule in (44) looks for the maximum output over the correlations between the received signal and all possible transmitted signals. If an exhaustive search is applied to find the maximum, the receiver has a worst case complexity of $O(M_T)$, which means the detection process will be prohibitively slow when L and M are large. Instead of correlating the whole received signal with the reference signals as in (44), an efficient receiver can be implemented using the correlation in each subpulse

$$x_{\bar{m},l} = \Re \left\{ \int_{(l-1)T}^{lT} \mathbf{h}^H \mathbf{r}_c(t) \phi_{\bar{m}}(t - (l-1)T) dt \right\}, \quad (71)$$

to formulate the matrix

$$\mathbf{X} = (x_{\bar{m},l}) \in \mathbb{R}^{(ML) \times L}. \quad (72)$$

The basis function $\phi_{\bar{m}}(t)$ is defined as

$$\phi_{\bar{m}}(t) = s_p(t) \exp(j(2\pi f_{n-1}t + \theta_m)),$$

where $\bar{m} \in \{1, 2, \dots, ML\}$ is the row index of the (\bar{m}, l) -th element in \mathbf{X} , $l \in \{1, 2, \dots, L\}$ is the column index of the (\bar{m}, l) -th element in \mathbf{X} which denotes the index of the subpulse, $n = \left(\lfloor \frac{\bar{m}-1}{M} \rfloor + 1\right) \in \{1, 2, \dots, L\}$ denotes the index of the frequency of the basis function $\phi_{\bar{m}}(t)$, $m = \left(\bar{m} - \lfloor \frac{\bar{m}-1}{M} \rfloor M\right) \in \{1, 2, \dots, M\}$ and $\theta_m = 2\pi(m-1)/M$ is the phase of $\phi_{\bar{m}}(t)$.

Then, we split \mathbf{X} into L^2 blocks of M elements whose basis functions have the same frequency and time slot. Using the maximum element in each block, we can formulate a new matrix, which can be expressed as

$$\mathbf{Y} = (y_{n,l}) \in \mathbb{R}^{L \times L}, \quad (73)$$

where

$$y_{n,l} = \max_{\bar{m} \in \{M(n-1)+1, \dots, Mn\}} x_{\bar{m},l}. \quad (74)$$

The row indices of $y_{n,l}$ in the original matrix \mathbf{X} is stored separately in $\bar{m}_{n,l}$. Note that the basis function used for $y_{n,l}$ is a complex exponential with frequency f_{n-1} . The worst case complexity of finding L^2 maximums in L^2 blocks is $O(L^2 \times M)$ if an exhaustive search is used.

To detect the frequency of each subpulse, we apply the Hungarian algorithm to \mathbf{Y} to select L elements \hat{r}_l , $l \in \{1, \dots, L\}$, such that these elements are in L different rows and L different

Algorithm 1 Hungarian Algorithm Based Method for the Communication Receiver

1: Formulate $\mathbf{X} = (x_{\bar{m},l}) \in \mathbb{R}^{(ML) \times L}$ using (71) and (72)
 2: **for** $l = 1$ to L **do**
 3: **for** $n = 1$ to L **do**
 4: $y_{n,l} \leftarrow \max_{\bar{m} \in \{M(n-1)+1, \dots, Mn\}} x_{\bar{m},l}$
 5: $\bar{m}_{n,l} \leftarrow \operatorname{argmax}_{\bar{m} \in \{M(n-1)+1, \dots, Mn\}} x_{\bar{m},l}$
 6: **end for**
 7: **end for**
 8: $\mathbf{Y} \leftarrow (y_{n,l}) \in \mathbb{R}^{L \times L}$
 9: Apply the Hungarian algorithm to matrix \mathbf{Y} following the steps in [22, algorithm 1] to get
 L elements \hat{r}_l and their row indices \hat{n}_l , where $l \in \{1, \dots, L\}$
 10: **for** $l = 1$ to L **do**
 11: Detection of the frequency of the l -th subpulse $\hat{f}_{l-1}^i \leftarrow f_{\hat{n}_{l-1}}$
 12: Detection of the phase of the l -th subpulse $\hat{\theta}_{l-1}^i \leftarrow \frac{2\pi \lfloor (\bar{m}_{\hat{n}_{l-1}} - 1)/M \rfloor}{M}$
 13: **end for**

columns, and the sum of the L elements is maximised. The detection of the frequency \hat{f}_{l-1}^i is determined by the row index \hat{n}_l of the selected element in the l -th column. Note that the Hungarian algorithm has a worst case time complexity of $\mathcal{O}(L^3)$ [32].

To detect the phase of each subpulse, we use the recorded indices $\bar{m}_{n,l}$ of the L elements selected by the Hungarian method. The detection of the phase $\hat{\theta}_{l-1}^i$ is determined by the row index of the selected element in the l -th column of the original matrix \mathbf{X} .

Algorithm 1 summarises the main steps of the Hungarian algorithm based communication receiver.

D. Numerical Examples

In this section we provide numerical examples to support the theoretical analysis of the communication performance in Section V-B. Fig. 9 to 11 illustrate the error probability of the waveform over different communication channel models. We mainly focus on the performance of the bounds and approximations derived in Section V-B.

Note that the analysis for correlated fading channels in Section V-B2 holds for all \mathbf{R}_u but in this section we use the simple exponential correlation model. Hence, given a correlation

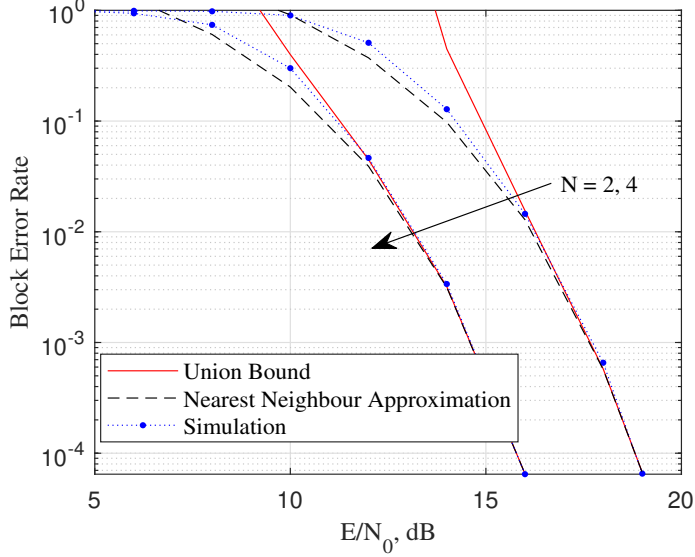


Fig. 9. The block error rate versus average received SNR for $L = 8$, $M = 4$ and $N = 2, 4$. The results are for the proposed baseband signalling model in an AWGN channel.

coefficient $\rho \in [0, 1]$, the (i, j) -th entry of \mathbf{R}_u can be written as

$$\mathbf{R}_u(i, j) = \rho^{|i-j|}. \quad (75)$$

Fig. 9 shows the block error rate versus the average received SNR in an AWGN channel with different number of receiver antennas, $N = 2, 4$. The parameters of the waveform are kept to be $L = 8$ and $M = 4$. The union bounds and nearest neighbour approximations are generated using (54) and (59). As expected, the block error rate decreases with an increase in N due to the receive diversity gain. The union bounds always stay above the corresponding simulation results and approach the simulation curves in the high SNR region. Compared to the union bounds, the nearest neighbour approximations provide better approximations to the simulation results, especially in the low SNR region.

Fig. 10 plots the block error rate versus the average received SNR in correlated Rician fading channels with different channel factors, $K = 0.25, 2.5, 10$. We set the waveform parameters, the number of receiving antennas and the correlation coefficient to be $L = 8$, $M = 4$, $N = 2$ and $\rho = 0.5$, respectively. As has been discussed, in the fading channel the union bounds are very loose. Thus, we only show the nearest neighbour approximations using (55) with the PEP and α_{1k}^{NN} provided in (62) and (57), respectively. The block error rate decreases with K , since the LOS component is increased. The nearest neighbour approximations accurately approximate the

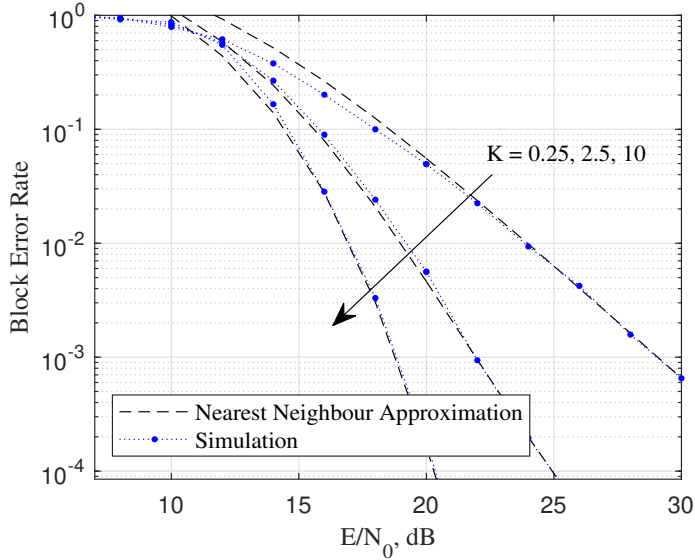


Fig. 10. The block error rate versus average received SNR for $L = 8$, $M = 4$ and $N = 2$. The results are for the proposed baseband signalling model in correlated Rician fading channels with $K = 0.25, 2.5, 10$ and $\rho = 0.5$.

corresponding simulation results in the high SNR region. However, the approximations become looser for smaller K in the low SNR region.

Fig. 11 plots the block error rate versus the average received SNR in a correlated Rayleigh fading channel with different numbers of receiver antennas, $N = 2, 4$. We set the waveform parameters and the correlation coefficient to be $L = 8$, $M = 4$ and $\rho = 0.5$, respectively. The new upper bounds in (70) are provided instead of the union bounds. The nearest neighbour approximations are generated using (55) with PEP and α_{1k}^{NN} provided in (63) and (57), respectively. Similar to what we observe in Fig. 9, the block error rate decreases with an increase in N . Also, the nearest neighbour approach approximates the simulation results more accurately with increasing N , especially in the low SNR region. The new upper bound is a tighter and more accurate performance bound on the block error rate compared to the union bound, which is not plotted in Fig. 11 since the value is always larger than 1. Therefore, for the proposed signalling scheme, the new upper bound does outperform the union bound over Rayleigh fading channels.

VI. CONCLUSION AND FUTURE EXTENSIONS

In this paper, we consider the integration of radar sensing and communications and propose a linear stepped frequency waveform and a frequency permutation based waveform, both with

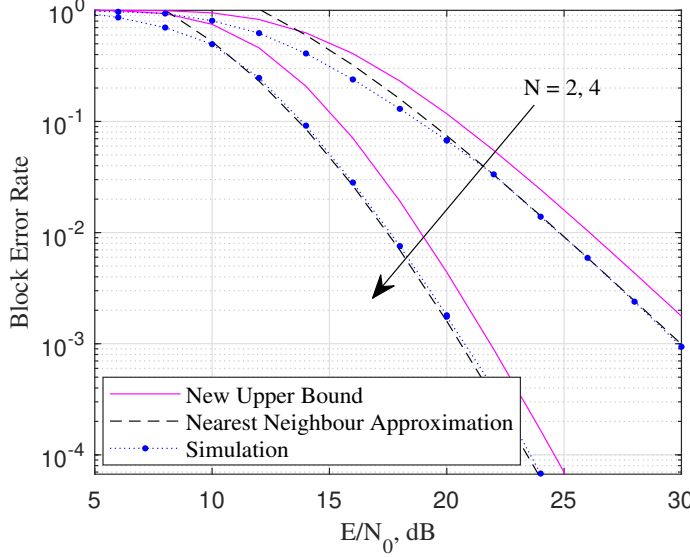


Fig. 11. The block error rate versus average received SNR for $L = 8$, $M = 4$ and $N = 2, 4$. The results are for the proposed baseband signalling model in correlated Rayleigh fading channels with $\rho = 0.5$.

phase modulation. Compared to modulating data using phase only, the randomisation in frequency tones in the second signalling scheme allows more data to be transmitted.

Focusing on the fundamental theoretical aspects, we analyse the effect of phase and frequency modulation on the radar sensing functionality and establish an important and fundamental theoretical result which shows that the phase modulation has negligible effect on the radar local accuracy. More specifically, we derive the AFs of both waveforms to analyse the impact of phase change on local accuracy and side-lobe levels. To provide quantitative measurements of the impact of phase modulation on the local accuracy, we also derive approximations to the CRLBs on delay and Doppler estimation errors based on the FIMs. We conclude that the frequency permutations result in reasonably low AF side-lobe level in average and the phase modulation has little impact on the local estimation accuracy. From the perspective of communications, we focus on analysing the block error probability of the phase modulated frequency permutation based waveform. We consider the optimal ML detection and derive the union bound and the nearest neighbour approximation on the block error rate over AWGN channels and correlated Rician fading channels. We also propose a new tighter upper bound on the block error probability, for which a closed-form expression is derived under the case of Rayleigh fading channels.

Possible future extensions of this work includes the quantitative analysis of the effect of

phase and frequency modulation on the side-lobe structure of the AF. From the communications perspective, it is desirable to extend the analysis to incorporate coding based on which a subset of possible waveforms can be selected to improve the error probability performance.

APPENDIX A

DERIVATION OF THE PAIRWISE ERROR PROBABILITY P_{1k} OVER RICIAN FADING CHANNELS

Using (60) and the unitary property of \mathbf{V} , we write $\mathbf{h}^H \mathbf{h}$ as

$$\begin{aligned} \mathbf{h}^H \mathbf{h} &= \left(\sqrt{\frac{K}{K+1}} \Delta^H + \sqrt{\frac{1}{K+1}} \mathbf{u}^H (\mathbf{R}_u^{1/2})^H \right) \left(\sqrt{\frac{K}{K+1}} \Delta + \sqrt{\frac{1}{K+1}} \mathbf{R}_u^{1/2} \mathbf{u} \right) \\ &= \left(\sqrt{\frac{K}{K+1}} \Delta^H \mathbf{V} + \sqrt{\frac{1}{K+1}} \mathbf{u}^H (\mathbf{R}_u^{1/2})^H \mathbf{V} \right) \left(\sqrt{\frac{K}{K+1}} \mathbf{V}^H \Delta + \sqrt{\frac{1}{K+1}} \mathbf{V}^H \mathbf{R}_u^{1/2} \mathbf{u} \right). \end{aligned} \quad (76)$$

Using (61), we reexpress $\sqrt{\frac{1}{K+1}} \mathbf{V}^H \mathbf{R}_u^{1/2} \mathbf{u}$ as

$$\sqrt{\frac{1}{K+1}} \mathbf{V}^H \mathbf{R}_u^{1/2} \mathbf{u} = \mathbf{D} \tilde{\mathbf{u}}, \quad (77)$$

where $\mathbf{D} = \sqrt{\frac{1}{K+1}} \mathbf{\Omega}^{1/2}$ is diagonal and $\tilde{\mathbf{u}} = \mathbf{V}^H \mathbf{u} \sim \mathcal{CN}(0, \mathbf{I}_N)$. Writing $\mathbf{D} = \text{diag}(d_1, \dots, d_N)$ where $d_j = \sqrt{\frac{\lambda_j}{K+1}}$, $j \in \{1, \dots, N\}$, we express (76) as

$$\begin{aligned} \mathbf{h}^H \mathbf{h} &= \left(\sqrt{\frac{K}{K+1}} \Delta^H \mathbf{V} + \tilde{\mathbf{u}}^H \mathbf{D}^H \right) \left(\sqrt{\frac{K}{K+1}} \mathbf{V}^H \Delta + \mathbf{D} \tilde{\mathbf{u}} \right) \\ &= \sum_{j=1}^N \left| \sqrt{\frac{K}{K+1}} (\mathbf{V}^H \Delta)_j + d_j \tilde{\mathbf{u}}_j \right|^2 \\ &= \sum_{j=1}^N \left(d_j \Re \{ \tilde{\mathbf{u}}_j \} + \sqrt{\frac{K}{K+1}} \Re \{ (\mathbf{V}^H \Delta)_j \} \right)^2 + \left(d_j \Im \{ \tilde{\mathbf{u}}_j \} + \sqrt{\frac{K}{K+1}} \Im \{ (\mathbf{V}^H \Delta)_j \} \right)^2, \end{aligned} \quad (78)$$

where $\tilde{\mathbf{u}}_j$ is the j -th element of $\tilde{\mathbf{u}}$, $(\mathbf{V}^H \Delta)_j$ is the j -th element of $\mathbf{V}^H \Delta$ and $\Im \{ \cdot \}$ denotes the imaginary part of the argument. We can further rewrite (78) as

$$\mathbf{h}^H \mathbf{h} = \sum_{j=1}^{2N} \nu_j (W_j - w_j)^2, \quad (79)$$

where $W_j \sim \mathcal{N}(0, 1)$,

$$\nu_j = \begin{cases} \frac{\lambda_j}{2(K+1)}, & 1 \leq j \leq N \\ \frac{\lambda_{j-N}}{2(K+1)}, & N+1 \leq j \leq 2N, \end{cases} \quad (80)$$

and

$$w_j = \begin{cases} -\sqrt{\frac{2K}{\lambda_j}} \Re \{(\mathbf{V}^H \Delta)_j\}, & 1 \leq j \leq N \\ -\sqrt{\frac{2K}{\lambda_{j-N}}} \Im \{(\mathbf{V}^H \Delta)_{j-N}\}, & N+1 \leq j \leq 2N. \end{cases} \quad (81)$$

With the expression of $\mathbf{h}^H \mathbf{h}$ in (79), we can now derive P_{1k} over the correlated Rician fading channel. Using (52) and conditioning on the distribution of $\mathbf{h}^H \mathbf{h}$, we express P_{1k} as

$$\begin{aligned} P_{1k} &= \mathbf{E}_{\mathbf{h}^H \mathbf{h}} \left[\Pr \left[Z > \frac{\sqrt{\mathbf{h}^H \mathbf{h}}}{\alpha_{1k}} \mid \mathbf{h}^H \mathbf{h} \right] \right] \\ &= \mathbf{E}_{\mathbf{h}^H \mathbf{h}} \left[Q \left(\frac{\sqrt{-\mathbf{h}^H \mathbf{h}}}{\alpha_{1k}} \right) \right], \end{aligned} \quad (82)$$

where $\mathbf{E}_X[\cdot]$ is the expectation of the argument with respect to the distribution of X . Using Craig's formula to reexpress the Gaussian Q-function, we write (82) as

$$P_{1k} = \frac{1}{\pi} \int_0^{\pi/2} \mathbf{E}_{\mathbf{h}^H \mathbf{h}} \left[\exp \left(\frac{\mathbf{h}^H \mathbf{h}}{2\alpha_{1k}^2 \sin^2 \theta} \right) \right] d\theta. \quad (83)$$

Substituting $\mathbf{h}^H \mathbf{h}$ with (79) we obtain

$$P_{1k} = \frac{1}{\pi} \int_0^{\pi/2} \prod_{j=1}^{2N} \mathbf{E}_{W_j} \left[\exp \left(-\frac{\nu_j (W_j - w_j)^2}{2\alpha_{1k}^2 \sin^2 \theta} \right) \right] d\theta. \quad (84)$$

Since $W_j \sim \mathcal{N}(0, 1)$, we rewrite the expectation in (84) as

$$\begin{aligned} \mathbf{E}_{W_j} \left[\exp \left(-\frac{\nu_j (W_j - w_j)^2}{2\alpha_{1k}^2 \sin^2 \theta} \right) \right] &= \int_{-\infty}^{\infty} \frac{1}{\sqrt{2\pi}} \exp \left(-\frac{\nu_j (W_j - w_j)^2}{2\alpha_{1k}^2 \sin^2 \theta} - \frac{W_j^2}{2} \right) dW_j \\ &= \sqrt{\frac{\alpha_{1k}^2 \sin^2 \theta}{\nu_j + \alpha_{1k}^2 \sin^2 \theta}} \exp \left(-\frac{\nu_j w_j^2}{2(\nu_j + \alpha_{1k}^2 \sin^2 \theta)} \right). \end{aligned} \quad (85)$$

Substituting (85), (80) and (81) into (84) and using some straight forward mathematical manipulations, we can obtain the expression of P_{1k} in (62).

APPENDIX B

DERIVATION OF THE CONDITIONAL PAIRWISE ERROR PROBABILITY \tilde{P}_{1k}

Using the results in (52) and (65), the PEP conditioned on $\mathbf{h}^H \mathbf{h} \geq \gamma$ can be expressed as

$$\tilde{P}_{1k} = \Pr[\sqrt{\mathbf{h}^H \mathbf{h}} < \alpha_{1k} Z \mid \mathbf{h}^H \mathbf{h} \geq \gamma], \quad (86)$$

where $Z \sim \mathcal{N}(0, 1)$. By conditioning on $\mathbf{h}^H \mathbf{h}$, (86) can be written as

$$\begin{aligned}\tilde{P}_{1k} &= \int_{\gamma}^{\infty} Q\left(\frac{\sqrt{x}}{\alpha_{1k}}\right) f_{\mathbf{h}^H \mathbf{h} | \mathbf{h}^H \mathbf{h} \geq \gamma}(x) dx \\ &= \int_{\gamma}^{\infty} Q\left(\frac{\sqrt{x}}{\alpha_{1k}}\right) \frac{f_{\mathbf{h}^H \mathbf{h}}(x)}{\Pr[\mathbf{h}^H \mathbf{h} \geq \gamma]} dx,\end{aligned}\quad (87)$$

where $f_{\mathbf{h}^H \mathbf{h}}(x)$ is the probability density function of $\mathbf{h}^H \mathbf{h}$. By applying Craig's formula to (87), we obtain the expression in (65).

APPENDIX C

DERIVATION OF THE J_{11} TERM

The derivation of the J_{11} term closely follows the steps in [22, Appendix B]. For convenience we provide the detailed derivation as follows.

We first derive $\overline{\omega^2}$ which is defined as

$$\overline{\omega^2} = \int_{-\infty}^{\infty} \omega^2 |S_i(\omega)| \frac{d\omega}{2\pi}, \quad (88)$$

where $S_i(j\omega)$ is the Fourier transform of the waveform $s_i(t)$ which can be expressed as

$$S(\omega) = \sqrt{\frac{T}{L}} \sum_{l=0}^{L-1} e^{j(-\theta_l^i - \omega_l T + (\omega_l - \omega) \frac{T}{2})} \text{sinc}\left((\omega - \omega_l) \frac{T}{2}\right). \quad (89)$$

Substituting (89) into (88) we have

$$\overline{\omega^2} = \frac{T}{2\pi L} \sum_{l=0}^{L-1} \sum_{n=0}^{L-1} e^{j((\theta_n^i - \theta_l^i) + (\omega_l - \omega_n) \frac{T}{2})} \int_{-\infty}^{\infty} \omega^2 e^{j\omega(n-l)T} \text{sinc}\left((\omega - \omega_l) \frac{T}{2}\right) \text{sinc}\left((\omega - \omega_n) \frac{T}{2}\right) d\omega \quad (90)$$

Due to the fact that the pulse shaping function $s_p(t)$ is a perfect rectangular pulse, $\overline{\omega^2}$ in (90) does not converge. In practice, pulses can never be perfectly rectangular since it requires an infinite bandwidth. Therefore, using the idea in [33], we assume that the bandwidth of the frequency spectrum of $s_p(t)$ is limited to a finite value of B Hz. As a result, (90) can be expressed as

$$\begin{aligned}\overline{\omega^2} &= \frac{T}{2\pi L} \sum_{l=0}^{L-1} \sum_{n=0}^{L-1} e^{j((\theta_n^i - \theta_l^i) + (\omega_l - \omega_n) \frac{T}{2})} \\ &\quad \times \int_{\omega_n - B\pi}^{\omega_l + B\pi} \omega^2 e^{j\omega(n-l)T} \text{sinc}\left((\omega - \omega_l) \frac{T}{2}\right) \text{sinc}\left((\omega - \omega_n) \frac{T}{2}\right) d\omega.\end{aligned}\quad (91)$$

For simplicity we let $v = \frac{\omega T}{2}$, $v_l = \frac{\omega_l T}{2}$ and $v_n = \frac{\omega_n T}{2}$. As a result, (91) can be reexpressed as

$$\overline{\omega^2} = \frac{4}{\pi L T^2} \sum_{l=0}^{L-1} \sum_{n=0}^{L-1} e^{j((\theta_n^i - \theta_l^i) + (v_l - v_n))} \int_{v_n - \frac{B\pi T}{2}}^{v_l + \frac{B\pi T}{2}} v^2 e^{j2vk} \text{sinc}(v - v_l) \text{sinc}(v - v_n) dv, \quad (92)$$

where $k = l - n$. By using the following equations

$$\frac{v^2}{(v - v_l)(v - v_n)} = 1 + \frac{v_l + v_n}{v - v_l} + \frac{v_n^2}{(v - v_l)(v - v_n)} \quad (93)$$

and

$$e^{j2vk} \text{sinc}(v - v_l) \text{sinc}(v - v_n) = \frac{1}{2} e^{j2vk} \cos(v_n - v_l) - \frac{1}{4} e^{j(2(k-1)v+v_l+v_n)} - \frac{1}{4} e^{j(2(k+1)v-v_l-v_n)}, \quad (94)$$

we can reexpress (92) as

$$\overline{\omega^2} = \frac{4}{\pi LT^2} \sum_{l=0}^{L-1} \sum_{n=0}^{L-1} e^{j((\theta_n^i - \theta_l^i) + (v_l - v_n))} I_{n,l}, \quad (95)$$

where

$$I_{n,l} = \int_{v_n - \frac{B\pi T}{2}}^{v_l + \frac{B\pi T}{2}} \left(1 + \frac{v_l + v_n}{v - v_l} + \frac{v_n^2}{(v - v_l)(v - v_n)} \right) \times \left(\frac{1}{2} e^{j2vk} \cos(v_n - v_l) - \frac{1}{4} e^{j(2(k-1)v+v_l+v_n)} - \frac{1}{4} e^{j(2(k+1)v-v_l-v_n)} \right) dv. \quad (96)$$

As is discussed in [22, Appendix B], the integrals in (96) are small and of order one when $k \neq 0, \pm 1$. Therefore, the only significant terms are $I_{n,n}$, $I_{n,n-1}$ and $I_{n,n+1}$, which can be expressed as

$$I_{n,n} = \frac{1}{4} \int_{v_n - \frac{B\pi T}{2}}^{v_l + \frac{B\pi T}{2}} \left(1 + \frac{2v_n}{v - v_n} + \frac{v_n^2}{(v - v_n)^2} \right) (2 - e^{j2(v_n - v)} - e^{j2(v - v_n)}) dv, \quad (97)$$

$$I_{n,n+1} = -\frac{1}{4} e^{j(v_n + v_{n+1})} \int_{v_n - \frac{B\pi T}{2}}^{v_l + \frac{B\pi T}{2}} \left(1 + \frac{v_n + v_{n+1}}{v - v_{n+1}} + \frac{v_n^2}{(v - v_n)(v - v_{n+1})} \right) dv + \mathcal{O}(1), \quad (98)$$

$$I_{n,n-1} = -\frac{1}{4} e^{j(v_n + v_{n-1})} \int_{v_n - \frac{B\pi T}{2}}^{v_l + \frac{B\pi T}{2}} \left(1 + \frac{v_n + v_{n-1}}{v - v_{n-1}} + \frac{v_n^2}{(v - v_n)(v - v_{n-1})} \right) dv + \mathcal{O}(1), \quad (99)$$

For large B , we can ignore the terms involving inverse powers of $v - v_n$, $v - v_{n+1}$ and $v - v_{n-1}$ as these are also order one. Therefore, we approximate $I_{n,n} \approx \frac{B\pi T}{2}$, $I_{n,n-1} \approx -\frac{B\pi T}{4} e^{j(v_n + v_{n-1})}$ and $I_{n,n+1} \approx -\frac{B\pi T}{4} e^{j(v_n + v_{n+1})}$. Substitute them into (95) and using some straightforward mathematical manipulations we obtain

$$\overline{\omega^2} \approx \frac{2B}{LT} \left(L - \sum_{l=0}^{L-2} \cos(\omega_l T + \theta_n^i - \theta_{n+1}^i) \right). \quad (100)$$

Next, we focus on $\bar{\omega}$ which is defined as

$$\bar{\omega} = \int_{-\infty}^{\infty} \omega |S_i(\omega)| \frac{d\omega}{2\pi}. \quad (101)$$

Following similar steps from (90) to (95), we reexpress (101) as

$$\overline{\omega^2} = \frac{2}{\pi LT} \sum_{l=0}^{L-1} \sum_{n=0}^{L-1} e^{j((\theta_n^i - \theta_l^i) + (v_l - v_n))} J_{n,l}, \quad (102)$$

where

$$J_{n,l} = \int_{v_n - \frac{B\pi T}{2}}^{v_l + \frac{B\pi T}{2}} \left(\frac{v_l}{(v - v_l)(v_l - v_n)} + \frac{v_n}{(v - v_n)(v_n - v_l)} \right) \times \left(\frac{1}{2} e^{j2vk} \cos(v_n - v_l) - \frac{1}{4} e^{j(2(k-1)v+v_l+v_n)} - \frac{1}{4} e^{j(2(k+1)v-v_l-v_n)} \right) dv. \quad (103)$$

Noting that all integrals in (103) are order one. Hence, for large B we can approximate

$$\bar{\omega} \approx 0. \quad (104)$$

Combining the results in (100) and (104) we can get the J_{11} term as given in (19).

APPENDIX D

DERIVATION OF THE J_{12} TERM

The derivation of the J_{22} term closely follows the steps in [22, Appendix C]. For convenience we provide the detailed derivation as follows.

From (104) we know that $\bar{\omega} \approx 0$. Thus, the J_{12} term can be approximated as

$$J_{12} \approx C\bar{\omega}\tau. \quad (105)$$

The definition of $\bar{\omega}\tau$ is given by

$$\bar{\omega}\tau = \Im \left\{ \int_{-\infty}^{\infty} ts_i(t) \frac{\partial s_i^*(t)}{\partial t} dt \right\}. \quad (106)$$

We denote the integral in (106) by Φ , which can be expressed as

$$\Phi = \int_{-\infty}^{\infty} ts_i(t) \frac{\partial s_i^*(t)}{\partial t} dt. \quad (107)$$

After some straightforward mathematical manipulations we can reexpress (107) as

$$\begin{aligned} \Phi &= \int_{-\infty}^{\infty} t \left(\sum_{l=0}^{L-1} s_p(t - lT) e^{j(\omega_l t + \theta_l^i)} \right) \\ &\quad \times \sum_{n=0}^{L-1} e^{-j(\omega_n t + \theta_n^i)} \left(\frac{\partial s_p(t - nT)}{\partial t} - j\omega_n s_p(t - nT) \right) dt. \end{aligned} \quad (108)$$

To calculate (108) we approximate $s_p(t)$ to be a smooth function which vanishes and has vanishing derivatives at endpoints $t = 0$ and $t = T$. To be more specific, we require

$$s_p(t)s_p(t - lT) = 0, \quad (109)$$

and

$$s_p(t) \frac{\partial s_p(t - lT)}{\partial t} = 0, \quad (110)$$

for any integer valued $l \neq 0$. As a result, (108) can be approximated as

$$\Phi \approx \sum_{l=0}^{L-1} \left(\int_{-\infty}^{\infty} ts_p(t - lT) \frac{\partial s_p(t - lT)}{\partial t} dt - j\omega_l \int_{-\infty}^{\infty} ts_p^2(t - lT) dt \right). \quad (111)$$

Substituting (111) into (106) we can approximate $\overline{\omega\tau}$ as

$$\overline{\omega\tau} \approx - \sum_{l=0}^{L-1} \omega_l \int_{-\infty}^{\infty} ts_p^2(t - lT) dt, \quad (112)$$

which can be further expressed as

$$\overline{\omega\tau} \approx -\frac{T^2}{2} \sum_{l=0}^{L-1} \omega_l (2l + 1). \quad (113)$$

Based on (113) we can obtain the J_{12} term as given in (20).

APPENDIX E

DERIVATION OF THE J_{22} TERM

The derivation of the J_{22} term closely follows the steps in [22, Appendix D]. For convenience we provide the detailed derivation as follows.

We first derive the expression of $\overline{\tau^2}$, which is defined as

$$\overline{\tau^2} = \int_{-\infty}^{\infty} t^2 |s_i(t)|^2 dt. \quad (114)$$

Substituting (31) into (114) we can get

$$\overline{\tau^2} = \frac{1}{LT} \sum_{l=0}^{L-1} \int_{lT}^{(l+1)T} t^2 dt = \frac{L^2 T^2}{3}. \quad (115)$$

Similarly, we can derive the expression of $\overline{\tau}$ which is defined as

$$\overline{\tau} = \int_{-\infty}^{\infty} t |s_i(t)|^2 dt. \quad (116)$$

Substituting (31) into (116) we can get

$$\overline{\tau} = \frac{1}{LT} \sum_{l=0}^{L-1} \int_{lT}^{(l+1)T} t dt = \frac{LT}{2}. \quad (117)$$

Combining (115) and (117) we can get the J_{22} term as given in (21).

REFERENCES

- [1] A. Hassanien, M. G. Amin, Y. D. Zhang, and F. Ahmad, "Signaling strategies for dual-function radar communications: an overview," *IEEE Aerosp. Electron. Syst. Mag.*, vol. 31, pp. 36—45, Oct. 2016.
- [2] C. Sturm and W. Wiesbeck, "Waveform design and signal processing aspects for fusion of wireless communications and radar sensing," *Proc. IEEE*, vol. 99, pp. 1236—1259.
- [3] L. Zheng and X. Wang, "Super-resolution delay-doppler estimation for OFDM passive radar," *IEEE Transactions on Signal Processing*, vol. 65, no. 9, pp. 2197—2210, 2017.
- [4] F. Liu, C. Masouros, A. P. Petropulu, H. Griffiths, and L. Hanzo, "Joint radar and communication design: Applications, state-of-the-art, and the road ahead," *IEEE Transactions on Communications*, vol. 68, no. 6, pp. 3834—3862, 2020.
- [5] J. A. Zhang, F. Liu, C. Masouros, R. W. Heath, Z. Feng, L. Zheng, and A. Petropulu, "An overview of signal processing techniques for joint communication and radar sensing," 2021.
- [6] A. Liu, Z. Huang, M. Li, Y. Wan, W. Li, T. X. Han, C. Liu, R. Du, D. T. K. Pin, J. Lu, Y. Shen, F. Colone, and K. Chetty, "A survey on fundamental limits of integrated sensing and communication," 2021.
- [7] D. K. Pin Tan, J. He, Y. Li, A. Bayesteh, Y. Chen, P. Zhu, and W. Tong, "Integrated sensing and communication in 6g: Motivations, use cases, requirements, challenges and future directions," in *2021 1st IEEE International Online Symposium on Joint Communications Sensing (JC&S)*, 2021, pp. 1—6.
- [8] D. Ma, N. Shlezinger, T. Huang, Y. Liu, and Y. C. Eldar, "Joint radar-communication strategies for autonomous vehicles: Combining two key automotive technologies," *IEEE Signal. Process. Mag.*, vol. 37, pp. 85—97, Jul. 2020.
- [9] P. Kumari, J. Choi, N. González-Prelcic, and R. W. Heath, "IEEE 802.11ad-based radar: An approach to joint vehicular communication-radar system," *IEEE Trans. Veh. Technol.*, vol. 67, pp. 3012—3027, Apr. 2018.
- [10] D. Tagliaferri, M. Rizzi, S. Tebaldini, M. Nicoli, I. Russo, C. Mazzucco, A. V. Monti-Guarnieri, C. M. Prati, and U. Spagnolini, "Cooperative synthetic aperture radar in an urban connected car scenario," in *2021 1st IEEE International Online Symposium on Joint Communications Sensing (JC&S)*, 2021, pp. 1—4.
- [11] X. Chen, Z. Feng, Z. Wei, F. Gao, and X. Yuan, "Performance of joint sensing-communication cooperative sensing UAV network," *IEEE Transactions on Vehicular Technology*, vol. 69, no. 12, pp. 15 545—15 556, 2020.
- [12] S. Zhang, Y. Zeng, and R. Zhang, "Cellular-enabled UAV communication: A connectivity-constrained trajectory optimization perspective," *IEEE Transactions on Communications*, vol. 67, no. 3, pp. 2580—2604, 2019.
- [13] P. Kumari, N. Gonzalez-Prelcic, and R. W. Heath, "Investigating the IEEE 802.11ad standard for millimeter wave automotive radar," in *IEEE Vehicular Technology Conference*, Boston, MA, USA, Sep. 2015, pp. 1—7.
- [14] P. Kumari, S. A. Vorobyov, and R. W. Heath, "Adaptive virtual waveform design for millimeter-wave joint communication-radar," *IEEE Transactions on Signal Processing*, vol. 68, pp. 715—730, 2020.
- [15] N. Levanon, "Multifrequency radar signals," in *Record of the IEEE 2000 International Radar Conference [Cat. No. 00CH37037]*. IEEE, 2000, pp. 683—688.
- [16] G. Lellouch, A. K. Mishra, and M. Inggs, "Stepped OFDM radar technique to resolve range and Doppler simultaneously," *IEEE Transactions on Aerospace and Electronic Systems*, vol. 51, no. 2, pp. 937—950, 2015.
- [17] C. Shi, F. Wang, M. Sellathurai, J. Zhou, and S. Salous, "Power minimization-based robust OFDM radar waveform design for radar and communication systems in coexistence," *IEEE Transactions on Signal Processing*, vol. 66, no. 5, pp. 1316—1330, 2018.
- [18] S. D. Blunt, P. Yatham, and J. Stiles, "Intrapulse radar-embedded communications," *IEEE Trans. Aerosp. Electron. Syst.*, vol. 46, pp. 1185—1200, Jul. 2010.

- [19] S. Dwivedi, A. N. Barret, P. Sen, and G. Fettweis, “Target detection in joint frequency modulated continuous wave (FMCW) radar-communication system,” in *2019 16th International Symposium on Wireless Communication Systems (ISWCS)*, pp. 277–282.
- [20] P. M. McCormick, C. Sahin, S. D. Blunt, and J. G. Metcalf, “FMCW implementation of phase-attached radar-communications (PARC),” in *2019 IEEE Radar Conference (RadarConf)*, 2019, pp. 1–6.
- [21] C. Sahin, J. Jakabosky, P. M. McCormick, J. G. Metcalf, and S. D. Blunt, “A novel approach for embedding communication symbols into physical radar waveforms,” in *2017 IEEE Radar Conference (RadarConf)*, 2017, pp. 1498–1503.
- [22] R. Senanayake, P. Smith, T. Han, J. Evans, W. Moran, and R. Evans, “Frequency permutations for joint radar and communications,” *arXiv preprint arXiv:2105.11106*, 2021.
- [23] M. Richards, *Fundamentals of Radar Signal Processing*, 2nd ed. McGrawHill Education, 2014.
- [24] N. Levanon and E. Mozeson, *Radar Signals*. John Wiley & Sons, Inc, 2004.
- [25] R. Frank, “Polyphase codes with good nonperiodic correlation properties,” *IEEE Transactions on Information Theory*, vol. 9, no. 1, pp. 43–45, 1963.
- [26] B. Lewis and F. Kretschmer, “A new class of polyphase pulse compression codes and techniques,” *IEEE Transactions on Aerospace and Electronic Systems*, vol. AES-17, no. 3, pp. 364–372, 1981.
- [27] I. P. Eedara, A. Hassanien, M. G. Amin, and B. D. Rigling, “Ambiguity function analysis for dual-function radar communications using PSK signaling,” in *2018 52nd Asilomar Conference on Signals, Systems, and Computers*, 2018, pp. 900–904.
- [28] H. L. VanTrees, *Detection, Estimation, and Modulation Theory: Radar-Sonar Processing and Gaussian Signals in Noise*. NY, USA: John Wiley & Sons, Inc, 2001.
- [29] D. Knuth, *The Art of Computer Programming, vol. 3: Sorting And Searching*. Addison-Wesley, 1973.
- [30] J. G. Proakis and M. Salehi, *Digital Communications*. NY, USA: McGraw-Hill, 2008.
- [31] N. L. Johnson, S. Kotz, and N. Balakrishnan, *Continuous Univariate Distributions, volume 2*. John wiley & Sons, Inc, 1970.
- [32] H. W. Kuhn, *The Hungarian Method for the Assignment Problem*. Wiley Online Library, 1955.
- [33] M. I. Skolnik, “Theoretical accuracy of radar measurements,” *IRE Transactions on Aeronautical and Navigational Electronics*, vol. 7, pp. 1960—1383, Dec. 1960.